KTH ROYAL INSTITUTE
OF TECHNOLOGY

Doctoral Thesis in Physics

Experimental Studies of Neutron Deficient Nuclei in the $A \approx 110$ and $A \approx 170$ Mass Regions

WEI ZHANG

Stockholm, Sweden 2022

Experimental Studies of Neutron Deficient Nuclei in the $A \approx 110$ and $A \approx 170$ Mass Regions

WEI ZHANG

Academic Dissertation which, with due permission of the KTH Royal Institute of Technology, is submitted for public defence for the Degree of Doctor of Philosophy on Thursday the 28th April 2022, at 3:00 p.m. in Kollegiesalen, Brinellvägen 8, Kungliga Tekniska Högskolan, Stockholm.

Doctoral Thesis in Physics
KTH Royal Institute of Technology
Stockholm, Sweden 2022

ISBN 978-91-8040-195-1
TRITA-SCI-FOU 2022:08

Printed by: Universitetsservice US-AB, Sweden 2022

Abstract

This doctoral thesis describes several experimental studies on the structures of neutron-deficient nuclei with mass numbers A≈110 and A≈170. The experiments were carried out at the Accelerator Laboratory of the University of Jyväskylä, Finland, using heavy-ion fusion-evaporation reactions induced by beams of energies around 5 megaelectronvolts/nucleon. The experimental setups used for these studies are based on the high-resolution germanium-detector array Jurogam in combination with the recoil ion separators RITU or MARA and their respective focal plane detector systems, as well as with other ancillary devices.

Using the recoil distance Doppler shift technique, lifetimes of excited states in the neutron-deficient osmium isotopes ^{169,171,173}Os were measured for the first time by coupling the Jurogam germanium detector array with the ancillary device DPUNS (differential plunger for unbound nuclear states), the gas-filled recoil separator RITU, and GREAT the decay spectrometer situated at the RITU focal plane. The differential decay curve analysis method was used to extract lifetimes of the excited states of interest. An anomalously low value was observed for the ratio of the reduced electric quadrupole transition probabilities between consecutive γ-ray transitions in the yrast band of ^{169}Os. This observation adds to the handful of nuclides known to exhibit such behavior, which cannot be explained by state-of-the-art theory. Based on data from the same experiment, new alpha decay fine structures were identified for the osmium isotopes ^{171,172}Os and iridium isotopes ^{171,172,174}Ir, relying on the correlations of the alpha decays with both prompt and delayed gamma rays. It is suggested that the relatively enhanced hindrance factors observed for some of the newly observed decays might be related to changes in the superposition degree of different geometrical shapes (shape coexistence) in the final-state wave functions of the respective daughter nuclei.

Another experimental setup used in the studies was based on the vacuum-mode mass separator MARA and its focal plane detector system in conjunction with the germanium array Jurogam and the charged-particle detector JYTube which was placed around the target position. In this work, the extremely neutron deficient proton emitting lanthanum isotope $^{116}_{57}$La was discovered. Enhanced proton emission probability and smaller proton-decay Q value were observed for ^{116}La compared with its nearest less neutron-deficient isotope ^{117}La. This unusual circumstance was proposed to be a possible effect of rarely observed neutron-proton pair correlations, as a result of their effect on the spatial distribution of the valence proton wave function.

Using the highly selective recoil-decay tagging technique, excited states in the extremely neutron-deficient tellurium isotope $^{107}_{52}$Te were identified from two independent experiments based on the two setups described above. The deduced level scheme was compared with shell model calculations and TRS (Total Routhian Surface) calculations, indicating that the valence neutron occupying the $h_{11/2}$ orbit has an important effect on the collectivity. The thesis includes two published articles and two manuscripts in advanced preparation. The experimental techniques and data analysis used in this work are

summarized and the theoretical background to the interpretations of the experimental results is briefly outlined.

Sammanfattning

Denna doktorsavhandling beskriver fyra experimentella studier av neutronfattiga atomkärnor med masstalen A≈110 och A≈170. Experimenten utfördes vid Acceleratorlaboratoriet vid universitetet i Jyväskylä, Finland, med användning av fusionsreaktioner inducerade av tungjonstrålar accelererade till energier av ca 5 megaelektronvolt/nukleon. De experimentuppställningar som används för dessa studier var baserade på germaniumdetektorsystemet Jurogam i kombination med rekylseparatorn RITU eller MARA och deras respektive fokalplansdetektorsystem, såväl som med andra tillhörande detektorsystem.

Med hjälp av Dopplerskiftsteknik uppmättes livstiderna för exciterade tillstånd i de neutronfattiga osmiumisotoperna ^{169,171,173}Os för första gången genom att kombinera detektorsystemet Jurogam med rekyljonseparatorn RITU, och detektorsystemet GREAT placerat vid RITUs fokalplan. Metoden för analys av differentiella sönderfallskurvor användes för att extrahera livstider för de exciterade tillstånden av intresse. Ett onormalt lågt värde observerades för förhållandet mellan de reducerade elektriska kvadrupolövergångssannolikheterna mellan på varandra följande övergångar i den starkaste gammakaskaden i ^{169}Os. Tidigare har endast en handfull nuklider observerats uppvisa sådant beteende vilket ej kan förklaras av vedertagna teoretiska modeller. Baserat på data från samma experiment identifierades finstrukturer i alfasönderfallen för osmiumisotoperna ^{171,172}Os och iridiumisotoperna ^{171,172,174}Ir, med hjälp av korrelationer mellan alfapartikelemission och fördröjd respektive omedelbar detektion av gammastrålning. Det föreslås att den reducerade övergångssannolikhet som observerades för vissa av dessa alfasönderfall kan relateras till effekter av att vågfunktionen i dotterkärnornas sluttillstånd antar en varierande superposition av olika geometriska former (”shape coexistence”).

En annan experimentell uppsättning som användes i studierna var baserad på rekylmasseparatorn MARA och dess fokalplansdetektorsystem i kombination med germaniumdetektorsystemet Jurogam och partikeldetektorn JYTube vilka var placerade runt strålmålet. I analysen av experimentdata upptäcktes den nya protonemitterande lantanisotopen ^{116}La. Ökad protonemissionssannolikhet och lägre sönderfallsenergi observerades för ^{116}La jämfört med den närmaste isotopen ^{117}La. Detta är oväntat och föreslås vara en möjlig effekt av att utökade parkorrelationer mellan neutroner och protoner i kärnan påverkar den spatiella fördelningen av valensprotonens vågfunktion.

Med hjälp av den mycket selektiva isotopidentifieringstekniken ”recoil decay tagging” observerades exciterade tillstånd i den extremt neutronfattiga atomkärnan ^{107}Te genom att kombinera data från två oberoende experiment. Experimenten genomfördes med de två olika detektoruppställningar som beskrivitss ovan. Det nivåschema som härleddes jämfördes med skalmodellberäkningar och TRS-medelfältsberäkningar vilket ledde till slutsatsen att när valensneutronen befinner sig i ett s.k. $h_{11/2}$ orbital har den en betydelsefull effekt på graden av kollektivitet i kärnans vågfunktion. Avhandlingen innehåller två publicerade artiklar och två manuskript. Experimentella tekniker,

dataanalysmetoder och den teoretiska bakgrunden till tolkningarna av experimentresultaten som använts i detta arbete beskrivs kortfattat i avhandlingen.

Acknowledgements

This thesis would not have been possible without the help of many people. First and foremost, I would like to thank my supervisor, Bo Cederwall, for giving me the opportunity to study at KTH nuclear physics group. I am deeply grateful for his inspiring guidance and ever continuing support, offering advice and encouragement with a perfect blend of insight and humor.

I wish to express my sincere gratitude to Chong Qi who has helped me a lot to improve my knowledge of nuclear theory and shared many interesting stories. My gratitude also extends to Özge Aktaş and Maria Doncel, especially for the help and encouragement at the beginning of my data analysis.

Sincere thanks are due to all the group members of nuclear physics at KTH for their patience and tolerance. It has been a great pleasure to share the office with Xiaoyu Liu, Ayşegül Ertoprak, Özge Aktaş, Linda Eliasson, Biswarup Das, and Arshiya Sood. Many thanks for the pleasant working environment they have created as well as for their friendship and immense helpfulness in different ways, also to my colleagues Jana Vasiljević and Ebba Ahlgren. I'm also very thankful for all the senior staff members, Torbjörn Bäck, Roberto Liotta, Ayse Ataç Nyberg and Ramon Wyss for discussions on various physics topics enabling me to deepen my understanding of nuclear physics.

Thanks also go to the collaborators for their valuable comments and suggestions on my work, special thanks to Jan Sáren and Juha Uusitalo at JYFL who helped me a lot with data analysis and patiently answered many of my questions about the experimental setups.

I am very grateful to the China Scholarship Council for giving me four years of financial support during my study at KTH.

Finally I wish to thank my family and my Huan for their support and encouragement throughout this period of my studies.

List of Publications

This thesis is based on the following four papers.

1. **Lifetime measurements of excited states in ^{169,171,173}Os: persistence of anomalous $B(E2)$ ratios in transitional rare earth nuclei in the presence of a decoupled $i_{13/2}$ valence neutron**
   W. Zhang, *B. Cederwall, M. Doncel, Ö. Aktas, A. Ertoprak, R. Liotta, C. Qi, T. Grahn, B.S. Nara Singh, D.M. Cullen, D. Hodge, M. Giles, S. Stolze, H. Badran, T. Braunroth, T. Calverley, D.M. Cox, Y.D. Fang, P.T Greenlees, J. Hilton, E. Ideguchi, R. Julin, S. Juutinen, M. Kumar Raju, H. Li, H. Liu, S. Matta, P. Subramaniam, V. Modamio, J. Pakarinen, P. Papadakis, J. Partanen, C.M. Petrache, P. Rahkila, P. Ruotsalainen, M. Sandzelius, J. Sarén, C. Scholey, J. Sorri, M.J. Taylor, J. Uusitalo, J.J. Valiente-Dobón*
   Phys. Lett. B **820**, 13627 (2021)

2. **Identification of excited states in $^{107}_{52}$Te$_{55}$**
   W. Zhang, *B. Cederwall, C. Qi, A. Ertoprak, Ö. Aktas, X. Liu, K. Andgren, K. Auranen, T. Bäck, L. Barber, G. Beeton, D. M. Cullen, I. G. Darby, M. R. Dimmock, S. Eeckhaudt, E. Ganioğlu, M. Górska, T. Grahn, P. T. Greenlees, B. Hadinia, E. Ideguchi, A. Illana, P. M. Jones, D. T. Joss, R. Julin, S. Juutinen, J. M. Keatings, A. Khaplanov, F. Kulali, M. Leino, M. Luoma, B. Lv, B.S. Nara Singh, L. Nelson, M. Niikura, M. Nyman, J. Ojala, R. D. Page, J. Pakarinen, E. S. Paul, C. Petrache, M. Petri, P. Rahkila, P. Ruotsalainen, M. Sandzelius, J. Sarén, C. Scholey, J. F. Smith, J. Sorri, H. Tann, G. Zimba, J. Uusitalo, R. Wadsworth, R. Wyss* Phys. Rev. C **104**, 064305 (2021)

3. **First observation of the proton emitter $^{116}_{57}$La$_{59}$: Evidence for strong isovector neutron-proton pairing from proton separation energies and emission probabilities**
   W. Zhang, *B. Cederwall, Ö. Aktas, J. Uusitalo, J. Sarén, X. Liu, A. Ertoprak, A. Ataç Nyberg, H. Badran, H. Boston, M. Doncel, U. Forsberg, T. Grahn, P. T. Greenlees, S. Guo, J. Heery, J. Hilton, D. Jenkins, R. Julin, S. Juutinen, M. Leino, M. Luoma, O. Neuvonen, J. Ojala, R. D. Page, J. Pakarinen, J. Partanen, E. S. Paul, C. Petrache, P. Rahkila, P. Ruotsalainen, M. Sandzelius, S. Szwec, H. Tann,*

R. Wadsworth
Submitted to Communications Physics

4. **Decay spectroscopy of ^{171,172}Os and ^{171,172,174}Ir**
W. Zhang, *B. Cederwall, M. Doncel, Ö. Aktas, A. Ertoprak, C. Qi, T. Grahn, B.S. Nara Singh, D.M. Cullen, D. Hodge, M. Giles, S. Stolze, K. Auranen, H. Badran, T. Braunroth, T. Calverley, D.M. Cox, Y.D. Fang, P.T Greenlees, J. Hilton, E. Ideguchi, R. Julin, S. Juutinen, M. Kumar Raju, M. Leino, H. Li, H. Liu, S. Matta, P. Subramaniam, V. Modamio, J. Pakarinen, P. Papadakis, J. Partanen, C.M. Petrache, P. Rahkila, P. Ruotsalainen, M. Sandzelius, J. Sarén, C. Scholey, J. Sorri, M.J. Taylor, J. Uusitalo, J.J. Valiente-Dobón*
To be submitted

Contents

title-1

Acknowledgements **vii**

List of Publications **ix**

Contents **xi**

List of Figures **xiii**

List of Tables **xvi**

List of Acronyms **xvii**

1 Introduction **1**

2 Theoretical Background **3**
- 2.1 Parametrisation of Nuclear Deformations 3
- 2.2 Alpha Decay 5
- 2.3 Proton Decay 9
- 2.4 Gamma Decay 9

3 Experimental Techniques **13**
- 3.1 Heavy-Ion Fusion Evaporation Reactions 13
- 3.2 Jurogam 14
- 3.3 Jyväskylä-York Tube 14
- 3.4 Ion Separators for Selection of Reaction Products 15
  - 3.4.1 Gas-Filled Recoil Separator RITU 16
  - 3.4.2 Vacuum-Mode Mass Separator MARA 17
- 3.5 Focal Plane Detector System of RITU 18
- 3.6 Focal Plane Detector System of MARA 20
- 3.7 DPUNS 21
- 3.8 Total Data Readout System 21

4 Data Analysis **25**
4.1 Calibration 25
4.2 Recoil Identification 25
4.3 Recoil Decay Tagging Technique 26
4.4 Identification of New Alpha Decays 28
4.5 Mass-to-Charge Ratios 28
4.6 Half-Life Measurements 30
4.7 Lifetime Measurements of Excited States 32
4.7.1 RDDS Method 32
4.7.2 DDCM Method 34

5 Summary **39**
5.1 Paper I 39
5.2 Paper II 39
5.3 Paper III 40
5.4 Paper IV 40
5.5 Author's Contributions 41

Bibliography **43**

List of Figures

2.1 Schematic diagram of the shape parameters in rotating quadrupole-deformed nuclei. The γ =60° axis corresponds to the non-collective oblate (rotation around the symmetry axis) shape, γ =0° to collective prolate (rotation perpendicular to the symmetry axis) shape, $\gamma = -60°$ to collective oblate and $\gamma = -120°$ to non-collective prolate shape. The figure is reproduced from Ref [1]. 4

2.2 Semiclassical picture of the potential energy of an alpha-residual nucleus system as a function of their separation distance. The solid and dashed curves display the cases where the angular momentum carried by the α-particle is zero or non-zero, respectively. 7

3.1 Schematic illustration of the fusion-evaporation reaction process. This figure is adapted from reference [17]. 13

3.2 Rendered design drawing of the Jurogam III germanium detector array, taken from reference [21]. 14

3.3 Picture of the charged particle detector array JYTube mounted in the target chamber, taken from reference [25]. 15

3.4 Schematic diagram for the RITU separator. The focusing quadrupole magnets and bending dipole magnet are indicated in the figure. The figure is taken from reference [28]. 16

3.5 Schematic diagram of the mass separator MARA. The ion optical elements, adjustable collimators, and m/q slit system are indicated. The figure is taken from reference [28]. 18

3.6 A schematic drawing of the GREAT spectrometer. 19

3.7 A schematic drawing of the focal plane detector system of MARA. The dashed line indicates the tilted focal plane, and the figure is reproduced from Ref. [30]. 21

3.8 A schematic drawing of the DPUNS plunger device, taken from Ref. [33]. 22

3.9 Schematic illustration of a typical TDR setup, with the individual time stamps of (a) the Jurogam detector, (b) the MWPC detector, and (c) the focal plane planar or clover germanium detector, relative to the software trigger event in the DSSD detector. Panel (d) shows the temporal structure after the individual signals are streamed together with respect to the starting time in DSSD by Grain. The figure is taken from [35] . . 23

4.1 Two-dimensional spectra used for identification of fusion-evaporation recoils. (a) Energy loss in the MWPC by recoils and scattered beamlike particles plotted against the time of flight between the MWPC and the DSSDs in the RITU experiment. (b) Energy deposited in the DSSD by recoils and scattered beam versus the time of flight in the MARA experiment. Recoil events are indicated by the shaded areas. 26

4.2 Prompt RDT γ-ray spectra from the ^{54}Fe(^{58}Ni, $2p3n$)^{107}Te reaction detected in the Jurogam III HPGe detector array at the target position. The fusion products were analyzed by the MARA separator and correlated with the characteristic α decays illustrating the selective power of the RDT technique. The cross section for this reaction is estimated to be $\sim 1\mu$b. The top panel shows the total γ-ray spectrum detected during the full experiment after recoil selection. The spectrum in the bottom panel is from events selected with an addtional tag on the characteristic alpha decay energy of ^{107}Te. 27

4.3 (a) $E_\alpha - E_\gamma$ coincidence spectrum with the time interval of $0 < \triangle t$ (γ - α) < 300 ns, where the delayed γ rays were detected by the planar detector at the focal plane and the α decays were measured with the DSSD. Each group is indicated with the corresponding energies, including the groups at the γ energies of 92.1 keV and 162.1 keV associated with the respective ^{171,172}Ir isotopes, and the group at α(5666 keV)-γ(136.1 keV) related to ^{173}Ir, as well as the groups at the γ energies of 43 keV and 73.6 keV correlated with the α decays of ^{169}Os. The parallelogram region indicates the newly identified α decays from the low-spin isomeric state of ^{172}Ir. (b) Projections on the E_α axis of the events from the ^{172}Ir region of (a) by gating on the respective delayed γ-ray. Relevant peaks are labeled with their corresponding E_α values. The intensity scale for the three weaker spectra is scaled up for better visibility. 29

4.4 Time difference spectrum between the ^{116}I recoil implantation and detection of its 227 keV isomeric-γ transition as well as a least-squares fit applied (solid green line) comprised of an exponential fit for the component of interest (blue dashed line) and an exponential fit for the background component (red dashed line). 31

4.5 Logarithmic time spectrum of the 5306 keV alpha decay events in correlation with ^{171}Os recoils, fitted with a two-component function (red). The time window for the recoil-α correlation was set to 1 min. The smaller distributions at higher ln($\triangle$t) values are due to the random correlated background with its effective fitted half-life. 33
4.6 A schematic illustration of the principle of the RDDS method, adapted from the reference [48]. 34
4.7 De-excitation scheme for coincidence DDCM. 36

List of Tables

2.1 Weisskopf single particle estimates. The transition probabilities T are in the unit of s^{-1}, A is the mass number and E_γ is the energy of the γ-ray in MeV. 10

2.2 Characteristic transition energy ratios and $B(E2)$ ratios for even-even Boson systems under the three symmetries of the IBM. A given nucleus with N_p valence protons and N_n valence neutrons (each calculated relative to the nearest magic number) has $N = (N_p + N_n)/2$ bosons [16]. 12

List of Acronyms

BGO	Bismuth Germanate
DDCM	Differential Decay Curve Method
DPUNS	Differential Plunger for Unbound Nuclear States
DSSD	Double-sided Silicon Strip Detector
GREAT	Gamma Recoil Electron Alpha Tagging spectrometer
HF	Hindrance Factor
HPGe	High-Purity Germanium
IBM	Interacting Boson Model
JYFL	Jyväskylän Yliopiston Fysiikan Laitos
JYTube	Jyväskylä-York Tube
MARA	Mass Analysing Recoil Apparatus
MWPC	Multiwire Proportional Counter
RDDS	Recoil Distance Doppler Shift
RDT	Recoil Decay Tagging technique
RITU	Recoil Ion Transport Unit
TDR	Total Data Readout system
ToF	Time-of-Flight
TRS	Total Routhian Surface
UDL	Universal Decay Law

Chapter 1

Introduction

The atomic nucleus is a unique quantum system of a finite number of strongly interacting particles (quarks) condensed into protons and neutrons. Since the confined quarks are Fermions, nucleons that consist of three quarks (uud for the proton and udd for the neutron) are also Fermions and hence obey the Pauli principle. This means that the total wave function of the composite nuclear system is antisymmetric with respect to the exchange of particles. One of the commonly assumed characteristics of nuclear quantum systems is that each nucleon in the atomic nucleus is confined to an individual orbit, analogous to that of an electron in an atom, and moves in the mean field generated by all the other nucleons. A single-particle excitation can therefore be described as the process of promoting a valence nucleon to an unoccupied orbital leading to a larger total energy of the nucleus. In addition, the coherent motion of many nucleons is expected to manifest itself as collective excitations such as rotations and vibrations. The overarching aim of nuclear physics is to reveal the effective interactions between the nucleons and to interpret nuclear phenomena, e.g., the origin of collective motion. Most of the known nuclides are unstable and are synthesized in the laboratory. The nuclear properties are highly sensitive to the number of protons and neutrons. A small change in the number of nucleons may introduce significant changes in the nuclear structure. This behavior is unique for finite quantum systems. On the other hand, the aforementioned collective modes are similar to those exhibited by macroscopic objects. This duality found in nuclear properties makes it appropriate to categorize nuclei as mesoscopic physical systems. Throughout the nuclear chart, an abundance of nuclear structures and modes of excitations can be found. However, neither the microscopic models nor the semiclassical pictures are able to provide a self-consistent description of experimentally observed phenomena, and the nucleon-nucleon interactions remain as a phenomenological concept.

In the last decades, advances in radioactive ion beam facilities, radiation detectors, and data acquisition electronics have brought impressive progress in the exploration of nuclear properties. Numerous new phenomena have been observed and the map of the nuclear chart has been expanded substantially. Experimental measurements on decay modes and observables such as angular momentum, lifetimes, binding energies, electromagnetic properties, etc., are of fundamental importance for improving our understanding of nuclear structure. In this thesis, the nuclei under study were produced in heavy-ion fusion reactions using accelerated ion beams from the JYFL Accelerator Laboratory, Finland. Lifetime measurements of the excited states in the neutron-deficient osmium isotopes have provided the most direct investigation of the emergence of collective behavior and deformation in this work. γ-spectroscopy identification of the excited states in the extremely neutron deficient ^{107}Te nucleus provided insights into the competition between the single-particle and collective motions. The observation of proton radioactivity for the extremely neutron-deficient ^{116}La nucleus contributes to the study of residual interactions between the valence neutron and proton. It may also provide new insights into the nature of nuclear superfluidity and the limits of nuclear existence. Alpha-decay fine structure, which was studied for some neutron deficient osmium and iridium nuclides in this work, presents a measure of the resemblance of the initial and final nuclear states during the decay process. It can provide valuable information on how spatially localized α-particle clusters are formed in the nucleus and probe subtle differences between the final-state wave functions in the daughter nucleus.

This thesis is divided into five chapters: following this Chapter, Chapter 2 briefly summarizes the theoretical background for understanding nuclear structure concepts linked to the subjects of interest in this thesis, Chapter 3 summarizes the details of the experimental instrumentation used in this work and the applied experimental techniques, Chapter 4 presents the related data analysis, and Chapter 5 summarizes the publications that form the basis of this thesis and the author's contributions.

Chapter 2

Theoretical Background

In order to gain knowledge of nuclear structure from experimental observations, we usually rely on theoretical models to bridge the gap to the microscopic sub-atomic scale. A large number of theoretical models of atomic nuclei have been developed for this purpose. In this chapter, a brief description of the models used in the thesis is presented.

2.1 Parametrisation of Nuclear Deformations

Atomic nuclei may accommodate energy either by means of single-particle excitations or by collective excitations, such as vibrations and rotations in which many nucleons are assumed to move together in a coherent way. Collective excitations in a spherical nucleus are due to small oscillations of the nuclear surface. If a deviation from spherical symmetry is induced by the valence nucleons, excited energy levels can be found as a result of vibrations or rotations around a deformed equilibrium. Based on observed excitation patterns, nuclei are also assumed to exhibit various shapes. In order to describe the nuclear shape degrees of freedom, the general approach is to parameterize its surface with a function that defines the radius by an extension of the spherical harmonics, $Y_{\lambda\mu}$, as

$$R(\theta,\varphi) = R_0 \left(1 + \sum_{\lambda=1}^{\infty} \sum_{\mu=-\lambda}^{\lambda} \alpha_{\lambda\mu} Y_{\lambda\mu}(\theta,\varphi) \right) \tag{2.1}$$

where R_0 is the radius of a spherical shape with the same volume as the deformed one, and $\alpha_{\lambda\mu}$ are the deformation coefficients. The first term, $\lambda = 0$, describes the change in nuclear volume and is usually omitted due to the approximate incompressibility of nuclear matter. The dipole term, $\lambda = 1$, indicates just a mere translation of the center of mass and is therefore not interesting for describing the internal properties of the nucleus. The terms $\lambda = 2$, $\lambda = 3$, and $\lambda = 4$ correspond to the quadrupole deformation, octupole deformation, and hexadecapole deforma-

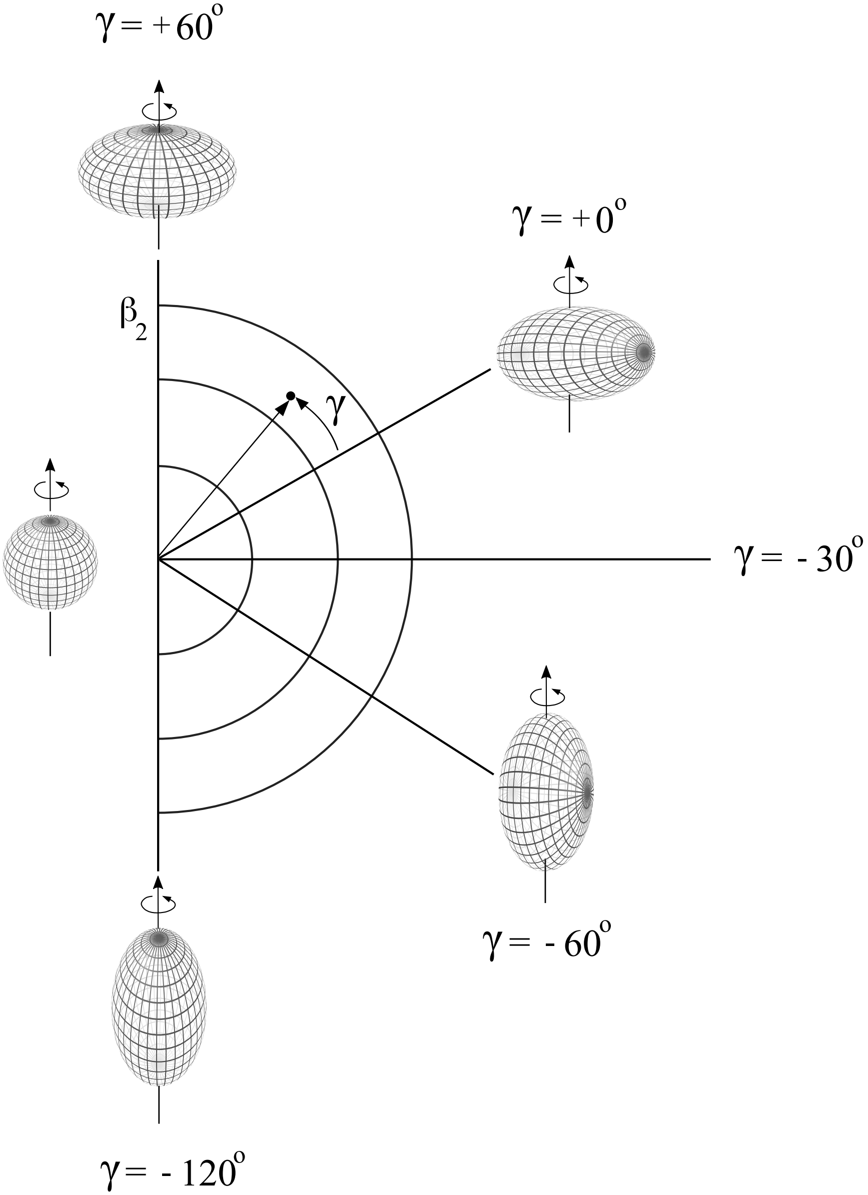

Figure 2.1: Schematic diagram of the shape parameters in rotating quadrupole-deformed nuclei. The γ =60° axis corresponds to the non-collective oblate (rotation around the symmetry axis) shape, γ =0° to collective prolate (rotation perpendicular to the symmetry axis) shape, $\gamma = -60°$ to collective oblate and $\gamma = -120°$ to non-collective prolate shape. The figure is reproduced from Ref [1].

tion, respectively, of which the quadrupole term is found to be the most common deformation type and the following of this thesis will focus on it. For convenience, the deformation in the intrinsic body-fixed system can be described by introducing the Hill-Wheeler coordinates β_2 and γ [2]. The coefficients $\alpha_{2\mu}$ of the quadrupole-deformed shape are then given as:

$$\begin{aligned} \alpha_{20} &= \beta_2 cos(\gamma) \\ \alpha_{2-2} = \alpha_{22} &= \frac{1}{\sqrt{2}}\beta_2 sin(\gamma) \end{aligned} \tag{2.2}$$

where the parameter β_2 stands for the degree of elongation or flattening of the nuclear shape and the parameter γ gives the degree of triaxial deformation [2]. The range of these parameters are $\beta_2 \geq 0$ and $-120^\circ < \gamma < +60^\circ$, as illustrated in Fig. 2.1. The corresponding parameterization in the body-fixed system can then be written as

$$R(\theta,\varphi) = R_0 \left(1 + \beta_2 \cos\gamma \; Y_{20}(\theta,\varphi) + \frac{1}{\sqrt{2}}\beta_2 \sin\gamma \; Y_{22}(\theta,\varphi)\right) \tag{2.3}$$

2.2 Alpha Decay

Alpha decay is a process in which a helium ion, with two protons and two neutrons, is emitted spontaneously from a nucleus, and can be written schematically as

$${}^{A}_{Z}X_N \rightarrow {}^{A-4}_{Z-2}Y_{N-2} + \alpha, \tag{2.4}$$

where A, Z, and N refer to the mass, proton, and neutron numbers of the mother nucleus, respectively. Alpha decay was first discovered in 1899 and identified in 1909 by Rutherford. Over the past century, α-decay measurements have been important for identifying new isotopes and elements, and for our understanding of nuclear structure. The principal alpha emitters are present in the neutron-deficient nuclei starting from mass number A ~150 and are abundant in heavy nuclei with atomic numbers greater than 83 [3]. In general, the energy release, Q_α, in α decays ranges from about 3 MeV to 10 MeV. The half-lives of alpha decays, ranging from μs to 10^{20} years, were found to have a striking correlation with the kinetic energies by Geiger and Nuttall, which was expressed phenomenologically as

$$\log_{10} T_{1/2} = A Q_\alpha^{-1/2} + B. \tag{2.5}$$

This relationship is called the Geiger-Nuttall law, in which the Z-dependent A and B coefficients are determined by fitting the experimental data and $T_{1/2}$ is the half-life for the α decay [4].

Microscopic Description of α Decay

In quantum models of α decay, the alpha particle is usually considered as a preformed cluster inside the mother nucleus prior to being emitted. The first microscopic, semiclassical, picture for describing the alpha emission process was proposed by Gamow in 1928 [5]: the preformed alpha particle is confined in a spherically symmetrical potential created by a combination of the attractive mean field potential and the Coulomb and centrifugal barriers, in which it moves independently and attempts frequently to escape. With the Wentzel-Kramers-Brillouin (WKB) approximation method for penetration (tunneling) through the potential barrier, the escape probability of an α-particle is:

$$P \propto exp(-2\int_{R_i}^{R_f} \sqrt{\frac{2\mu}{\hbar^2}(V(r)-Q_\alpha)}\,dr), \tag{2.6}$$

where μ is the reduced mass of the α-daughter system, the distance parameters R_i and R_f correspond to the respective internal and external turning points, and $V(r)$ is the potential by the superposition of the alpha-nuclear potential and the Coulomb and centrifugal barriers. A common potential used to calculate the penetration probability P was proposed by Rasmussen [6] as

$$V(r) = -1100 \times exp[-\frac{r-1.17A^{1/3}}{0.574}] + \frac{2Ze^2}{4\pi\epsilon_0 r} + \frac{\hbar^2}{2\mu r^2} l(l+1), \tag{2.7}$$

where the exponential expression is the nuclear interaction potential between the alpha particle and the residual daughter nucleus which is valid around the surface of the daughter nucleus [7], A is the mass number of the mother nucleus and Ze is the charge on the daughter nucleus, l is the orbital angular momentum of the emitted alpha particle, and r is the distance between the alpha particle and the daughter nucleus in fermis. A one-dimensional schematic drawing of the α-emission process can be seen in Fig. 2.2. Then the decay constant λ_α can be calculated by multiplying the penetration probability P by the impact frequency f of α-decay, as

$$\lambda_\alpha = fP \tag{2.8}$$

where the impact frequency f of an α-particle colliding with the potential barrier can be estimated as $f = v/R_i$, and v is the relative velocity of the alpha particle moving inside the nucleus.

The Gamow theory omitted the preformation process of the α particle, which is needed in evaluating the absolute decay width. A fully microscopic treatment of the α decay process was developed by Thomas [8], within the R-matrix theory. An alternative simplified transformation of the Thomas expression for the decay width can be written [9]

$$\begin{aligned} \Gamma_l = \frac{\hbar}{\tau} &= \frac{\hbar^2 R}{\mu} P_l(R) |\mathcal{F}_l(R)|^2 \\ P_l(R) &= \frac{kR}{|H_l^+(R)|^2} \end{aligned} \tag{2.9}$$

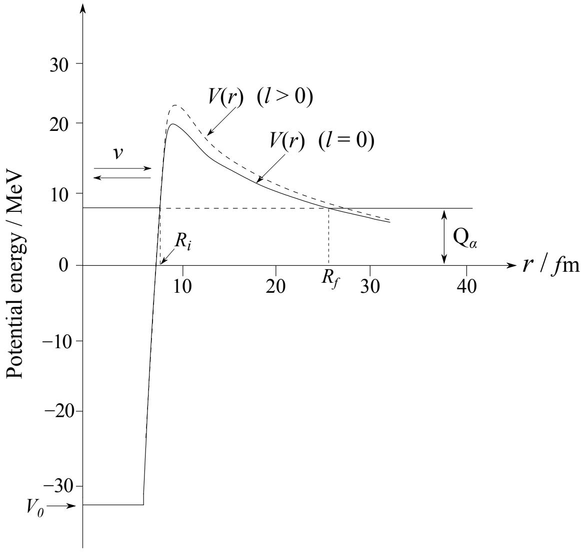

Figure 2.2: Semiclassical picture of the potential energy of an alpha-residual nucleus system as a function of their separation distance. The solid and dashed curves display the cases where the angular momentum carried by the α-particle is zero or non-zero, respectively.

where l represents the decay channel, k is the momentum of the α-particle, R is the distance between the α-particle and the residual nucleus at which the α-particle is already formed, $\mathcal{F}_l(R)$ is the formation amplitude at the distance R, and $P_l(R)$ is the penetrability through the Coulomb and centrifugal barriers starting at the point R, and $H_l^+(R)$ corresponds to the outgoing Coulomb-Hankel wave function [10,11]. The formation amplitude $\mathcal{F}_l(R)$ is the overlap between the mother nucleus and the product of the daughter nucleus and the α particle wave functions

$$\mathcal{F}_l(R) = \int d\xi_d d\xi_\alpha dr[\Psi_d(\xi_d)\Phi_\alpha(\xi_\alpha)Y_l(r)]^*\Psi_m(\xi_m). \tag{2.10}$$

Universal Decay Law

Using equation 2.9, the formation amplitude can be extracted from the expression [11]

$$log|R\mathcal{F}_l(R)| = \frac{1}{2}log[\frac{ln2}{v}|H_l^+(R)|^2] - \frac{1}{2}logT_{1/2}. \tag{2.11}$$

Analogous to the analytical WKB expression, the outgoing Coulomb-Hankel function can be approximated as [10]

$$\begin{aligned} H_l^+(R) &\approx C_l(\chi,\rho)(cot\beta)^{1/2}\ exp[\chi(\beta - sin\beta\ cos\beta)]] \\ C_l(\chi,\rho) &= exp\ [\frac{l(l+1)}{\chi} tan\beta] \\ cos^2\beta &= \frac{\rho}{\chi}, \end{aligned} \tag{2.12}$$

where $\rho = kR$ and $\chi = 2Z_d Z_\alpha e^2/\hbar v$ with the outgoing velocity v, Z_d and Z_α the charge numbers of the daughter nucleus and the α-particle cluster. The distance R is estimated by the typical form, i.e., $R = 1.2(A_d^{1/3} + A_\alpha^{1/3})fm$ with A_d and A_α being the mass number of the daughter nucleus and $A_\alpha = 4$, and the effects of the centrifugal barrier are fully included in $C_l(\chi,\rho)$. Then, the formation amplitude can be evaluated directly from the experimental observables Q and $T_{1/2}$.

In addition, a generalization of the Geiger-Nuttall law can be obtained by defining the quantities $\chi' = Z_\alpha Z_d \sqrt{A_{d\alpha}/Q_\alpha}$ and $\rho' = \sqrt{A_{d\alpha} Z_\alpha Z_d (A_d^{1/3} + A_\alpha^{1/3})}$ with $A_{d\alpha} = A_d A_\alpha/(A_d + A_\alpha)$, in which the decay half life is in the formula of

$$logT_{1/2} = a\chi' + b\rho' + c, \tag{2.13}$$

where a, b, c are constants to be determined [11]. This generalized formula is called the Universal Decay Law (UDL) since it can hold for all cluster radioactivities and the fitted coefficients a, b, and c do not depend on the atomic number Z as in the Geiger-Nuttall law [12].

Alpha Fine Structure and Hindrance Factor

Alpha decay can not only proceed from the initial state of the mother nucleus to the ground state of the daughter nucleus, but also to the excited states of the daughter nucleus. This gives rise to the well-known α-decay fine structure. The fine structure can give valuable information for the determination of the configurations in both the initial and final states. In order to evaluate the structural change, the hindrance factor was introduced by Rasmussen as the ratio between the reduced decay widths for decays to the ground state and excited state [6], that is

$$HF = \frac{\delta^2(\text{ground state} \rightarrow \text{ground state decay})}{\delta^2(\text{ground state} \rightarrow \text{excited state decay})} \tag{2.14}$$

where the reduced decay width is defined as $\delta^2 = \frac{\lambda h}{P}$ which is to remove the dependence upon the Q-value and only to concentrate on the nuclear structure of the daughter nucleus. For determining the HF value for the alpha-decay of odd-Z and odd-A nuclei, the ground-state to ground-state alpha decay of the nearest even-even nucleus is usually chosen as the reference, and in many cases, the ground-state α-decay of ^{212}Po is also a common reference. An alternative expression of the hindrance factor is given by the ratio between two α-particle formation amplitudes related to two different decay paths to the daughter nucleus [10].

$$HF = \left| \frac{\mathcal{F}(\text{ground state} \rightarrow \text{ground state decay})}{\mathcal{F}(\text{ground state} \rightarrow \text{excited state decay})} \right|^2 . \tag{2.15}$$

2.3 Proton Decay

Proton radioactivity is a rare nuclear decay mode and it was not discovered until around 50 years ago. Due to the very low production cross-sections, only about 50 proton decaying states, the ground or isomeric states of odd-Z extremely neutron-deficient nuclides [13], have been observed so far. At the proton drip line, the neutrons are no longer able to provide enough binding energy for all the protons, making the nucleus energetically unstable which eventually emits a proton. The current techniques limit the lifetimes for detecting proton decay to more than 10^{-7} s. Then the Coulomb and centrifugal barriers have to provide conditions for confining the proton inside the nucleus long enough. Knowledge of the proton emission energy and the half-life of the proton decaying state can provide important information on the nuclear structure. Analogous to the process of α decay, proton decay can also be separated into two steps as shown in Eq. 2.9, in which the formation probability reflects the proton resonance and the similarity of nuclear structure between mother nucleus and daughter nucleus [10].

2.4 Gamma Decay

The probability for γ-ray emission in an atomic nucleus is determined by the energy difference $\triangle$E between the initial and final states, the multipolarity L, and the change in parity $\triangle\pi$. These conditions are directly associated with the nature of the nuclear wave functions $|I_i\rangle$ and $|I_f\rangle$ for the respective initial and final states. The transition should obey the angular momentum quantum number inequality [4]

$$|I_i - I_f| \leq L \leq |I_i + I_f| \tag{2.16}$$

and the conservation of the total parity. For an electric transition, the parity change is given by

$$\pi_i \cdot \pi_f = (-1)^L \tag{2.17}$$

and for a magnetic transition the parity change by

$$\pi_i \cdot \pi_f = (-1)^{L+1}. \tag{2.18}$$

When the nucleus emits a γ-ray deexciting from a state of angular momentum I_i to a state of I_f, the total transition probability can be determined by [14]

$$T_{if} = \frac{8\pi(L+1)}{\hbar L[(2L+1)!!]^2} (\frac{E_\gamma}{\hbar c})^{2L+1} B(\lambda L, I_i \rightarrow I_f) \tag{2.19}$$

where the $B(\lambda L)$ is known as the reduced transition probability which reflects the nuclear structure information and is independent on the transition energy. The values of $B(\lambda L)$ are given by

$$B(EL, I_i \rightarrow I_f) = \frac{1}{2I_i + 1} |\,\langle f|\,|\hat{Q}_L|\,|i\rangle\,|^2, \tag{2.20}$$

for the electric case, and

$$B(ML, I_i \rightarrow I_f) = \frac{1}{2I_i + 1} |\,\langle f|\,|\hat{M}_L|\,|i\rangle\,|^2 \tag{2.21}$$

for the magnetic case, in which $\hat{Q}_L$ and $\hat{M}_L$ are the respective electric and magnetic multipole operators for the description of the produced electromagnetic radiation field during the γ-emission.

Weisskopf Estimates

With the assumption that the transition is due to a single proton de-exciting from one single-particle state to another state in a spherical basis, the transition probabilities Eq. 2.19 can be simplified to a large extent, as listed in Table. 2.1 for the transition probabilities of the lower multipole orders. This is known as Weisskopf estimates [4]. Apparently, these estimates are quite limited and not realistic calculations of the transition probabilities, but they can provide good rough comparisons with the experimental measurements. For instance, these estimates can provide reasonable relative comparisons of electromagnetic transition rates and allow one to make some general predictions about which multipole is most likely to be emitted [4]. Moreover, if the measured transition rate value is much higher than the value of Weisskopf estimate for a given multipolarity, then it is indicated that there is more than one nucleon involved in the transition and a collective process is observed. Weisskopf estimates are therefore commonly used as an alternative unit of the measured transition rates for revealing collective behavior.

Table 2.1: Weisskopf single particle estimates. The transition probabilities T are in the unit of s^{-1}, A is the mass number and E_γ is the energy of the γ-ray in MeV.

ML transitions	EL transitions
$T(M1) = 5.6 \times 10^{13} {E_\gamma}^3$	$T(E1) = 1.0 \times 10^{14} A^{2/3} {E_\gamma}^3$
$T(M2) = 3.5 \times 10^{7} A^{2/3} {E_\gamma}^5$	$T(E2) = 7.3 \times 10^{7} A^{4/3} {E_\gamma}^5$
$T(M3) = 1.6 \times 10^{1} A^{4/3} {E_\gamma}^7$	$T(E3) = 3.4 \times 10^{1} A^{2} {E_\gamma}^7$

Collective $E2$ Transition Probabilities

The collective electric and magnetic transition probabilities have been deduced by Bohr and Mottelson within the rotational model [14]. In this work, we only focus on the $E2$ transition probability, and the reduced $E2$ transition probability is given by

$$B(E2, I \rightarrow I-2) = \frac{5}{16\pi} e^2 Q_0^2 < IK20 \mid I-2K >^2, \tag{2.22}$$

where the expression in the bracket is the Clebsch-Gordan coefficient connecting the initial state $|I>$ and the final state $|I-2>$, and the intrinsic quadrupole moment Q_0 can be expressed in terms of the deformation,

$$Q_0 = \frac{3}{\sqrt{5\pi}} R_0^2 Z\beta(1+0.16\beta), \tag{2.23}$$

with Z being the proton number [14]. It is noteworthy that the transformation from the reduced transition probability $B(E2)$ as an observable quantity to the intrinsic quadrupole moment Q_0 is only valid when the $E2$ transitions are from within a rotational band in which the states have the same intrinsic wave functions. For Eq. 2.19, the $E2$ transition rate is given by

$$T(E2) = 1.22 \times 10^9 E_\gamma^5 B(E2). \tag{2.24}$$

By means of lifetime measurements, one is able to determine the $B(E2)$ values,

$$B(E2\downarrow) = \frac{0.0816}{E_\gamma^5(1+\alpha)\tau} \left[\ e^2b^2\ \right], \tag{2.25}$$

where α is the internal conversion coefficient for the $E2$ transition which can be taken from Ref. [15], E_γ is the transition energy in MeV, and τ is the extracted lifetime of the state of interest in picoseconds.

To evaluate the evolution of shape and collective behavior (rotational or vibrational) as the angular momentum increases within a collective band structure, one can perform the analysis in terms of some characteristic quantities, such as the energy ratio of the $E2$-transitions and the ratio of the $B(E2)$ values. The Interacting Boson Model (IBM) specific for collective behavior can well describe the low excitation properties of nuclei [16]. This model has three dynamical symmetries: U(5), SU(3) and O(6), corresponding to the spherical vibrator, prolate rigid rotor, and triaxial rotor, respectively. For each limit, the characteristic quantities are shown in Table 2.2.

Table 2.2: Characteristic transition energy ratios and $B(E2)$ ratios for even-even Boson systems under the three symmetries of the IBM. A given nucleus with N_p valence protons and N_n valence neutrons (each calculated relative to the nearest magic number) has $N = (N_p + N_n)/2$ bosons [16].

IBA	$\frac{E_{4^+}}{E_{2^+}}$	$\frac{B(E2;4^+\to 2^+)}{B(E2;2^+\to 0^+)}$
U(5)	2.0	$2(1-\frac{1}{N})$
SU(3)	3.33	$\frac{10}{7}\frac{(N-1)(2N+5)}{N(2N+3)}$
O(6)	2.5	$\frac{10}{7}\frac{(N-1)(N+5)}{N(N+4)}$

Chapter 3

Experimental Techniques

3.1 Heavy-Ion Fusion Evaporation Reactions

The experiments described in this work have been carried out at the heavy-ion accelerator facility at the University of Jyväskylä, Finland. The fusion-evaporation reaction is the most effective and commonly employed mechanism to populate nuclear states with high angular momentum. In a heavy-ion induced fusion evaporation reaction, the nucleus of interest is produced by bombarding the accelerated ions on the isotopically enriched target materials from a few MeV up to several tens of MeV per nucleon. After the projectiles pass through the Coulomb barrier, two heavy ions may fuse together, generally leading to a neutron-deficient compound nucleus that remains together long enough for the excitation energy to be equilibrated among all the constituent nucleons. The compound nucleus is a system at high temperature, which will start to evaporate protons, neutrons, and alpha particles until the excitation energy becomes lower than the binding energy for the particles. After particle evaporation, the deexcitation of the final nucleus proceeds mainly via γ radiation. The whole process is shown schematically in Figure. 3.1.

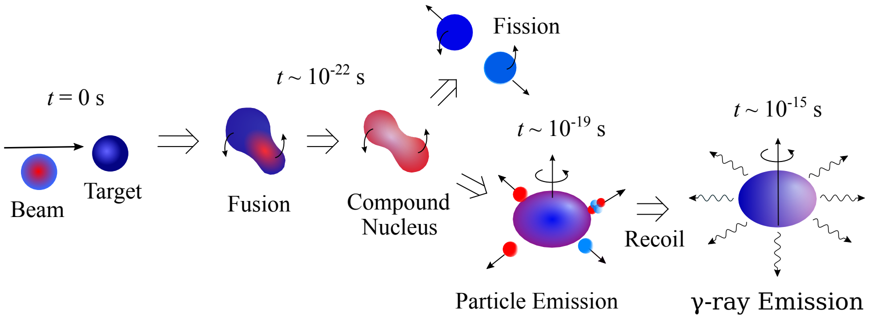

Figure 3.1: Schematic illustration of the fusion-evaporation reaction process. This figure is adapted from reference [17].

3.2 Jurogam

Three generations of germanium detector arrays, Jurogam I, II, and III, were used to detect prompt γ rays at the target position in different experiments. All of them are comprised of high-purity germanium detectors and each detector is individually Compton-suppressed by means of a bismuth germanate (BGO) scintillator shield. Jurogam I consisted of 43 coaxial detectors of either GASP [18] or Eurogam Phase1 [19] type. Jurogam II and III were upgraded from Jurogam I and consisted of 15 Eurogam Phase I-type [19] and 24 Euroball clover [20] escape-suppressed detectors, with a total photopeak efficiency of ∼5% at 1.3 MeV. The clover detectors were arranged symmetrically around the target position relative to the plane perpendicular to the beam direction (twelve at 75.5° and twelve at 104.5°), while the Phase I detectors were placed at backward angles with respect to the beam direction (five at 157.6° and ten at 133.6°) [21].

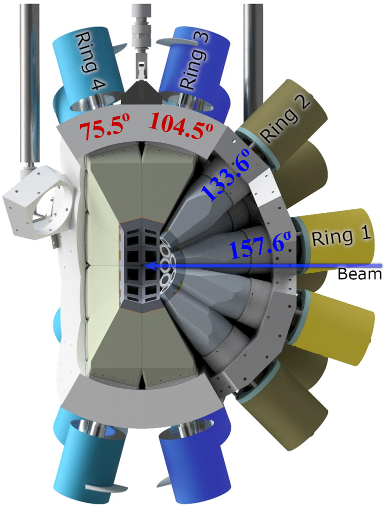

Figure 3.2: Rendered design drawing of the Jurogam III germanium detector array, taken from reference [21].

3.3 Jyväskylä-York Tube

The charged particle detector array JYTube was placed at the target position and resided in the LISA (Light Ion Spectrometer Array) target chamber [22]. It has six sides and is divided into two barrels. As shown in Fig. 3.3, these two hexagonal barrels are combined together around the target position. The JYTube is comprised of 96 independent plastic scintillator detectors. Each detector consists of an Eljen plastic scintillator with a size of 20 × 20 × 2 mm coupled to a prism-shaped perspex light guide and joined to a square SiPM (Silicon Photo Multiplier) readout [23]. The JYTube is used to detect charged particles, alpha particles and protons, which could help to select the evaporation reaction channel. Its detection efficiency for one proton is around 80% [24]. This detector was applied in the ^{107}Te and ^{116,117}La experiments, especially in the latter one, it played a critical role in identifying the new isotope ^{116}La with the requirement that ≤ 1 charged particle was detected for events leading to La fusion residues. However, in neither experiment was it possible to distinguish different types of charged particles. In addition, JYTube can be used as a veto detector, and for instance, its veto efficiency for triple charged-particle emission can be as high as 97%, and therefore it can enhance the selection of weak neutron-evaporation channels very effectively.

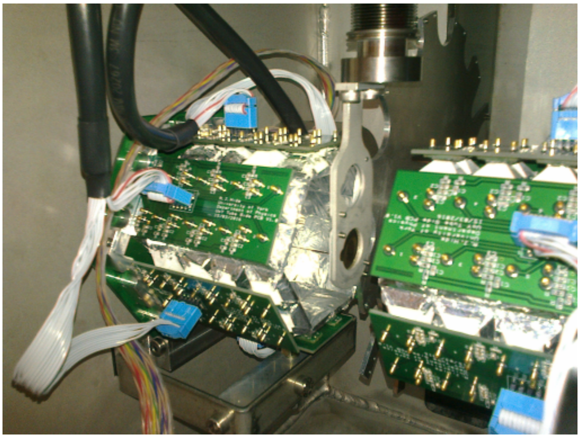

Figure 3.3: Picture of the charged particle detector array JYTube mounted in the target chamber, taken from reference [25].

3.4 Ion Separators for Selection of Reaction Products

Recoil separators are the primary devices for studying the production and decay properties of reaction products. They can transmit the fusion residues to the focal plane detector system in the downstream direction with a transmission time on the order of 1 μs. They can also separate the recoils from unreacted beam particles and scattered target-like nuclei in flight. All separators are usually comprised of different electromagnetic elements such as electric dipoles, magnetic dipoles, and magnetic quadrupoles. Dipoles are used to achieve recoil separation and magnetic quadrupole lenses are used to accomplish ion focusing. There are two types of separators available at JYFL, a gas-filled separator RITU and a vacuum-mode separator MARA. Both of them have been used in this work.

3.4.1 Gas-Filled Recoil Separator RITU

RITU operates in a QDQQ configuration [26], where Q stands for a quadrupole magnet and D represents a dipole magnet. Compared to the standard DQQ configuration, the first quadrupole magnet in front of the dispersive dipole provides a vertically focusing effect for better matching the dipole magnet acceptance, which leads to an increase to around 30% in transmission [27]. The total length of RITU is 4.8 m and its schematic layout is shown in Fig. 3.4.

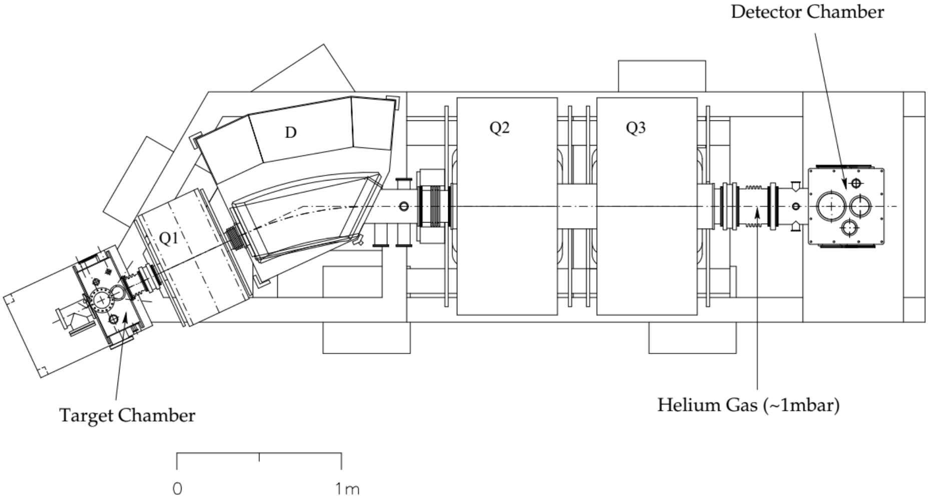

Figure 3.4: Schematic diagram for the RITU separator. The focusing quadrupole magnets and bending dipole magnet are indicated in the figure. The figure is taken from reference [28].

According to the deflection principle of charged particles moving in a magnetic field, the dipole magnet is responsible for separating the recoils from the beam particles. The use of a gas-filled dipole magnet can collect more charge states to increase the transmission efficiency, but at the cost of losing mass resolving power. In some favorable reactions, the transmission efficiency of RITU can reach as high as 50%. At the exit from the thin target, recoils have a wide distribution of charge states. In collisions with the gas atoms in the dipole magnet, the recoiling ions of a certain species reach a velocity-dependent charge equilibration and the corresponding mean flight trajectory will be determined by the average charge state q_{av}. Usually, the helium gas is the practical choice for filling the magnet cavity and the optimum pressure is maintained at a certain level of 1 mbar in order to minimize the implantation image size at the focal plane [26].

The degree of separation of the fusion residues can be roughly estimated by the magnetic rigidity formula [29]

$$B\rho = mv/eq_{av} \approx \frac{mv}{[(v/v_0)eZ^{1/3}]} = 0.0227\frac{A}{Z^{1/3}}[Tm] \tag{3.1}$$

where B is the magnetic field strength produced by the dipole magnet, ρ is the curvature radius of the ion trajectory, m, v, A, Z are the mass, velocity, mass number, and velocity of the ion, respectively. This formula is approximately valid in the $1 < v/v_0 < Z^{2/3}$ velocity region where q_{av} is approximated by $(v/v_0)eZ^{1/3}$ using the Thomas-Fermi model [14], of which v_0 is the Bohr velocity $2.19{\times}10^6$ m/s. It can be seen that the magnetic rigidity is independent of the charge state and velocity of the ions. When the $\frac{A}{Z^{1/3}}$ values of fusion residues are sufficiently different from that of the scattered target-like nuclei and beam particles, the separator works excellently, particularly in asymmetric reactions.

3.4.2 Vacuum-Mode Mass Separator MARA

MARA is a new recoil separator complementary to the RITU separator, and it was commissioned in the year 2016. RITU has been successfully applied to the research on heavy neutron deficient elements (transition-lead region). However, it becomes challenging to study lighter and medium-heavy elements (A up to around 150) with this device. One reason for this is that to produce these lighter elements one has to use symmetric or near-symmetric reactions, and it is more difficult to suppress the primary beam in such reactions. Secondly, the relative cross-section of the reaction channel of interest in symmetric reactions is usually very small and the absolute production cross section can be on the order of nb or less. This makes it highly desirable to identify the nuclei using a separator with a mass resolving power. The mass separator MARA is intended to work in the mass region below A = 150 and can separate the fusion products from unreacted beam particles more effectively in symmetric reactions, besides it can physically separate the fusion products based on their mass to charge (m/q) ratio [30].

MARA has an asymmetric $QQQED$ ion-optical configuration, where Q refers to a quadrupole magnet, E refers to an electrostatic deflector and D represents a dipole magnet. The quadrupole triplet is responsible for focusing the fusion products in both the horizontal and vertical directions; on one hand, it focuses the reaction products from the target to the deflector in a point-to-parallel manner; on the other hand, it focuses the reaction products from the target to the focal plane in a point-to-point manner. The role of the deflector is to separate the primary beam particles from the reaction products based on the different electric rigidities [30]. The reaction products are separated from each other according to different energies per charge while flying through the deflector. The magnetic dipole is used to create the mass dispersion and cancel the energy dispersion defocused by the deflector to achieve an energy focus at the focal plane. The total length of MARA along the optical axis is 6.85 m. An overview diagram of MARA is shown in Fig. 3.5. Its transmission efficiency is about 10 $\sim$ 40% and is related to the electric and magnetic field intensities as translated into the parameter settings such as the reference particle and charge states acceptance. Generally, it can be set to collect ions with 2 to 5 charge states. The best first-order resolving power of MARA can reach 250 at the focal plane [31].

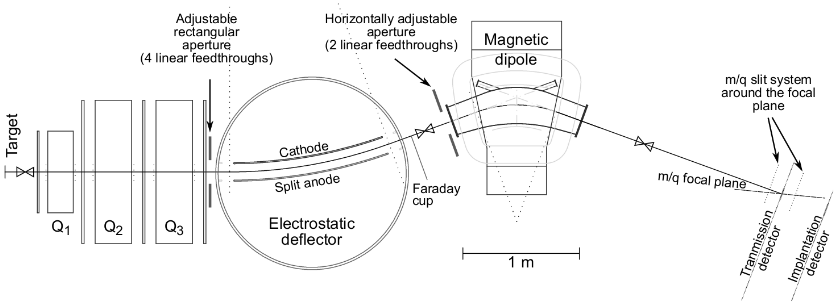

Figure 3.5: Schematic diagram of the mass separator MARA. The ion optical elements, adjustable collimators, and m/q slit system are indicated. The figure is taken from reference [28].

3.5 Focal Plane Detector System of RITU

The GREAT spectrometer is placed at the focal plane of the RITU gas-filled separator [32]. It is a composite system designed for measuring the radioactive properties of the transported reaction products. It consists of an MWPC, two DSSDs, an array of 28 silicon PIN photodiode detectors, as well as a double-sided planar germanium strip detector, and three clover-type germanium detectors. A schematic drawing of the GREAT spectrometer is shown in Figure. 3.6.

MWPC

The MWPC detector is positioned at the entrance of the GREAT spectrometer [32]. Its aperture is 131mm horizontally and 50mm vertically, and the isobutane working gas is filled and kept at a constant pressure of ~3.5 mbar. Two 0.9 μm Mylar foil windows are mounted at the inlet and outlet of the MWPC, respectively. The window at the outlet is used to separate the working gas isobutane from the vacuum chamber housing the other detectors, while the entrance window is used to separate the working gas from the helium gas of RITU. The principal functions of the MWPC are to record the energy loss and timing signals, and also provide position information during ion transmission. In conjunction with the DSSDs, the fusion reaction products can be cleanly distinguished from their subsequent radioactive decays and the scattered beam particles.

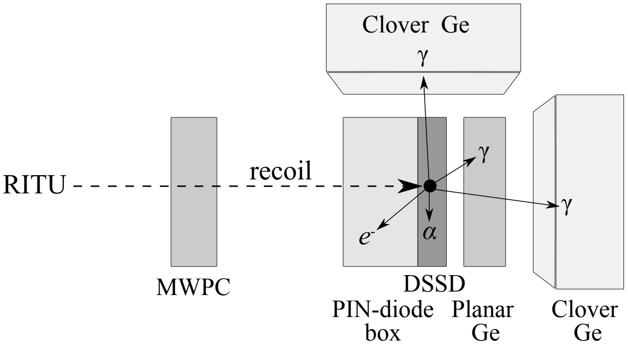

Figure 3.6: A schematic drawing of the GREAT spectrometer.

DSSD Implantation Detectors

The transported reaction products are deposited into two DSSDs positioned side by side. The DSSDs will record the relevant information, including their energies and times, and those of their subsequent charged-particle decays [32]. To obtain the best energy resolution and suppress the effects of radiation damage, the DSSDs are cooled to around -20°, which is achieved by using a recirculating refrigeration system. Each DSSD is 300 μm thick and has an effective area of 60×40 mm^2 with silicon strips placed orthogonally on the opposite faces. The strip pitch is 1 mm, so each DSSD gives a total of 2400 independent quasi-pixels. The high granularity enables high implantation rates and long correlation search times between the implantation and its subsequent decay. However, it is often not possible to achieve both goals simultaneously, as high implantation rates can only be allowed when the half-life of the nucleus of interest is short enough, and vice versa. Therefore the upper limit of the correlation time is mainly dependent on the research objectives, otherwise, a large number of random correlations will be introduced. Conversely, the lower limit of correlation time can reach an order of 10 μs, which is due to the response time of the electronics to process a signal pulse. Although the active channel is insensitive to other events during this busy phase, the rest of the detector continues to function normally. A way to access short half-lives of less than 10 μs is to apply a fast digital data acquisition system to the preamplifier of the DSSD, which digitizes the preamplifier output signal at a high 40 MHz sampling rate. The shape of the pileup signal can be thus resolved from the traces, and short half-lives, ≤ 10 μs, can be analyzed. Then the lower half-life limit is determined by the flight time through the ion separators. The active areas of the two DSSDs are estimated to typically cover ~85% of the reaction products reaching the RITU focal plane. The detection efficiency of the DSSDs for α decays is usually around ~55% depending on the recoil implantation depth, because there is a significant probability of decay particles escaping in the backward direction.

Silicon PIN Photodiode Detectors

The PIN photodiodes are cooled by the same refrigeration system as the DSSDs and mounted in a box arrangement around the perimeter of the DSSDs in the upstream direction [32]. They are used to collect charged particles escaped backward from the DSSD and to measure conversion electrons from highly-converted delayed or isomeric transitions. Each of the 28 PIN diodes is 500 μm thick, with a 28×28 mm^2 active area, and the combined array has a geometrical efficiency of about 30%.

Planar Germanium Strip Detector

A planar double-sided germanium strip detector is mounted behind the DSSDs approximately 10 mm downstream with an active area of 120×60 mm^2. It is designed to provide high-resolution and efficient measurements for low-energy photons (in the energy range of 10 keV to 200 keV) and high-energy charged particles which traversed the DSSDs. It is 15 mm thick and has a 0.5 mm thick beryllium entrance window. The strip pitch is 5 mm on both sides providing sensitive position information to allow events to be spatially correlated with the DSSD pixels.

Clover Germanium Detector

The Clover germanium detectors of GREAT are used to measure γ-rays emitted at the focal plane. They are mounted on three different faces around the GREAT vacuum chamber in a closely packed geometry. Each Clover detector comprises four high-purity germanium crystals and each crystal has 70 mm in diameter and 105 mm long before shaping. An escape suppression BGO shield surrounds each Clover detector to improve the peak to total ratio. Together with the planar detector, it is highly efficient in measuring any delayed or isomeric γ-rays emitted from the implanted fusion products.

3.6 Focal Plane Detector System of MARA

A similar detector system to the GREAT spectrometer is employed at the focal plane of MARA [24]. It is composed of an MWPC, a DSSD and a second layer of silicon, as well as five clover-type germanium detectors, as shown schematically in Figure. 3.7. Compared to RITU, the focal plane of MARA has a larger active area because it has a 20% higher solid angle acceptance. The MWPC consists of three wire planes, x-plane, cathode, and y-plane. The wire planes are made of 20 μm diameter gold-plated tungsten wire with 1 mm spacing between wires. In addition to giving a timing signal, the x-plane of MWPC also provides the spatial position of the fusion product implantation and gives the m/q information. A 300 μm thick DSSD of model BB20 was placed 40 cm behind the MWPC. It has 72 strips on the y-plane and 192 strips on the x-plane, each with a width of 0.67 mm. The second layer of silicon comprises two 500 μm thick silicon detectors mounted in parallel and

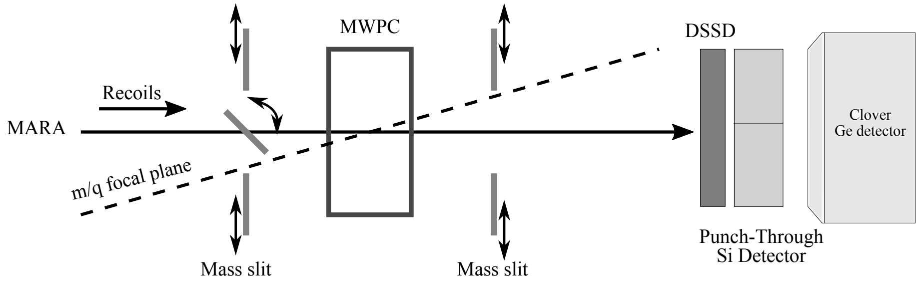

Figure 3.7: A schematic drawing of the focal plane detector system of MARA. The dashed line indicates the tilted focal plane, and the figure is reproduced from Ref. [30].

adjacently behind the DSSD to identify the punch-through events. In this work, they were used to act as a veto detector to reject the particles that escaped from the DSSD and did not deposit their full energy. Moreover, as illustrated in Figure 3.7, a double-mass slit system is introduced at the focal plane at the entrance and at the exit of the MWPC, which is used to select how many charge states of a given mass to be transported into the focal plane.

3.7 DPUNS

The Differential Plunger for Unbound States (DPUNS) apparatus [33] was designed based on the Köln Plunger design [34] to work in the gas environment of RITU. This device was installed at the center of the Jurogam array at the target position, and usually the degrader foil is placed in the exact center and the target is moved relative to the degrader to change the target-to-degrader distance. In this work, DPUNS was used for measuring lifetimes of the excited states in picoseconds using the recoil distance Doppler shift method which will be described in section 4.7.1. A schematic drawing of the mechanical design of DPUNS is shown in Figure 3.8. The piezoelectric stepper motor was connected to the target and controlled to move the target position with a precision of less than 0.1 μm. The role of the piezoelectric actuator was to keep the target-to-degrader distance constant during beam impinging on the target. A more detailed explanation of this device can be found in Ref. [33].

3.8 Total Data Readout System

The total data readout (TDR) system is a triggerless data acquisition system, which reads out all of electronic signals from each detector independently. Data from each detector are time-stamped to a precision of 10 nanoseconds using a 100 MHz global

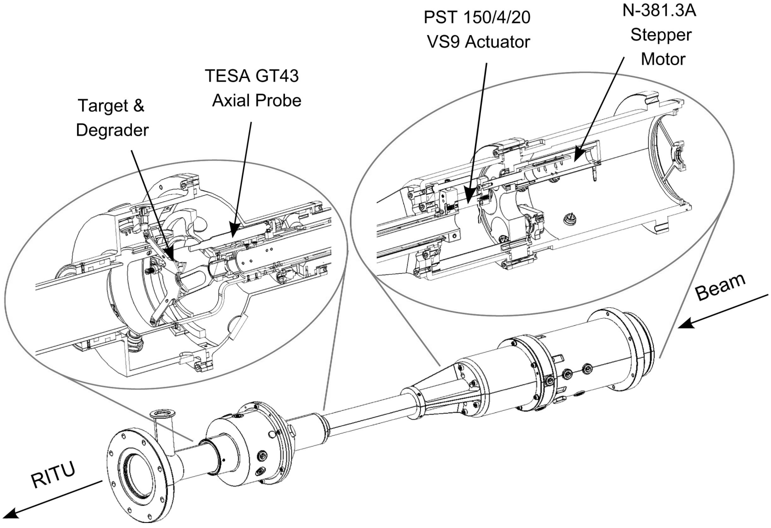

Figure 3.8: A schematic drawing of the DPUNS plunger device, taken from Ref. [33].

clock. The data is reconstructed using the Grain software package [35] and analyzed on-line or off-line. Temporal and spatial correlations to sort events out of the raw data as well as the filtering process to remove unwanted or irrelevant data were done entirely in the Grain software. Figure 3.9 shows a description of the typical TDR time structure, where every signal in the implantation detector DSSD is considered as a starting time for an event.

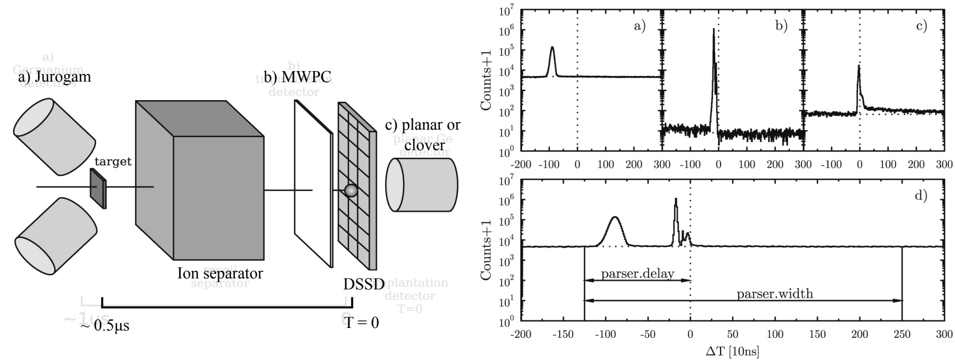

Figure 3.9: Schematic illustration of a typical TDR setup, with the individual time stamps of (a) the Jurogam detector, (b) the MWPC detector, and (c) the focal plane planar or clover germanium detector, relative to the software trigger event in the DSSD detector. Panel (d) shows the temporal structure after the individual signals are streamed together with respect to the starting time in DSSD by Grain. The figure is taken from [35]

Chapter 4

Data Analysis

4.1 Calibration

Energy calibration of each detector is usually the first step in the data analysis. The process is to align the energy spectra from different detectors by gain matching the ADC (Analog to Digital Converter) channels to the known energies that come from standard radioactive sources or from in-beam data of known nuclei. Calibration runs with the standard sources were performed both before and after each experiment. For the germanium detectors at the target position and at the focal plane, the standard radioactive γ-ray sources ^{152}Eu and ^{133}Ba were used for the energy calibration. Also the efficiency calibration can be achieved for the JUROGAM detectors by normalizing the detected intensities of γ rays to the corresponding intensities emitted by the source using an energy-dependent efficiency function. However, determining the detection efficiency of the Ge detectors at the focal plane has to additionally rely on the results of Monte Carlo simulations because the actual recoil distribution varies depending on experimental conditions and deviates strongly from an ideal point source distribution.

A mixed-element source (^{244}Cm, ^{241}Am, and ^{239}Pu) with its three main alpha lines was used to calibrate the DSSDs. In practical situations, the measured α energies from the implanted fusion products are often slightly larger than the energies obtained from the calibration coefficients on account of the dead layer at the surface of the detector and the kinetic energy of the recoiling daughter nucleus (which, however, is subject to the well known pulse height defect [36]). Therefore, it has to be corrected by applying an additional internal calibration using known α energies emanating from known reaction products.

4.2 Recoil Identification

Although the separators already suppressed the primary beam to a large extent, some scattered beam particles or target-like particles are transported to the focal plane. In the offline analysis, there are two alternative methods to further screen the reaction products from the scattering particles. One method is by their energy-loss in the MWPC ($\triangle$E) and the time-of-flight (ToF) between the MWPC and DSSD. The other method is by using the correlation between the deposited energy in the DSSD (E) and the ToF. As illustrated in the two-dimensional spectra shown in Fig. 4.1, the recoils are cleanly separated from the scattered beam components. By applying a two-dimensional gate on the identified recoils, we can select the prompt γ-rays produced immediately after the fusion reactions and the subsequent decays associated with the fusion products.

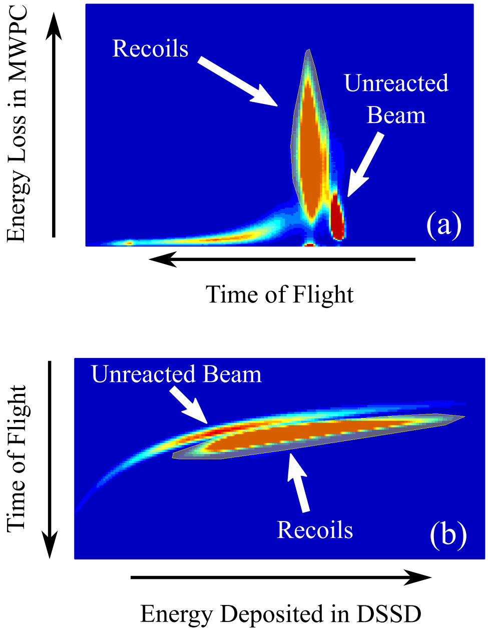

Figure 4.1: Two-dimensional spectra used for identification of fusion-evaporation recoils. (a) Energy loss in the MWPC by recoils and scattered beamlike particles plotted against the time of flight between the MWPC and the DSSDs in the RITU experiment. (b) Energy deposited in the DSSD by recoils and scattered beam versus the time of flight in the MARA experiment. Recoil events are indicated by the shaded areas.

4.3 Recoil Decay Tagging Technique

After the recoil events are identified, one can correlate them with the corresponding prompt γ rays collected by the Jurogam HPGe detector array surrounding the target. Using prompt γ rays, level schemes can be established by recoil-γ-γ matrix or by recoil-γ-γ-γ cube coincidence analysis. In a heavy-ion fusion evaporation experiment, a large number of open reaction channels are typically produced. However, the cross-section for producing the reaction channel of interest is often weak and the associated prompt γ-rays will be buried in the "background" created by the more prolific reaction products. Once the recoils are implanted into the focal plane DSSD, the time, position and implantation energy can be recorded. The subsequent decays are also registered in the DSSD with their time, position and energy, but decays unlike recoils produce no signal in the MWPC. In light of the decay providing characteristic information, the decay can be used as a selective tag on the nucleus of interest. By correlating the implanted recoil with its signature decay spatially and temporally, the prompt γ-rays associated with the recoil can be unraveled. This method is known as recoil-decay-tagging (RDT) [37].

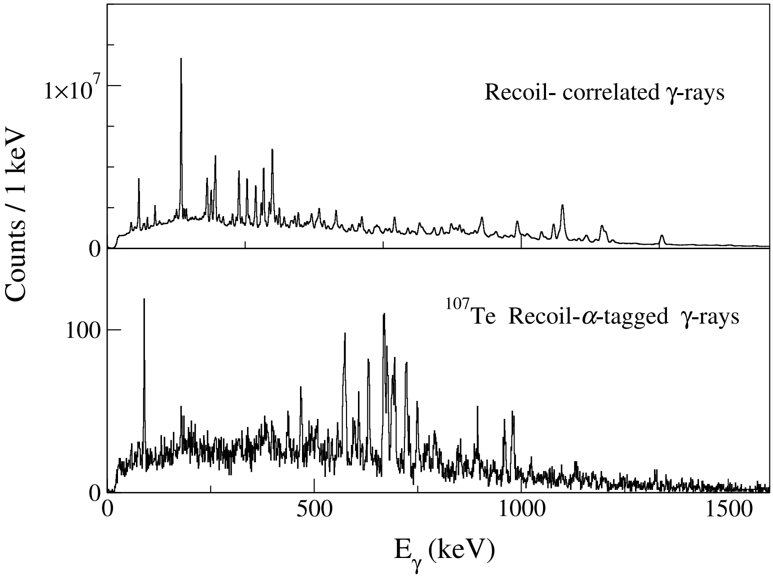

Figure 4.2: Prompt RDT γ-ray spectra from the ^{54}Fe(^{58}Ni, $2p3n$)^{107}Te reaction detected in the Jurogam III HPGe detector array at the target position. The fusion products were analyzed by the MARA separator and correlated with the characteristic α decays illustrating the selective power of the RDT technique. The cross section for this reaction is estimated to be $\sim 1\mu$b. The top panel shows the total γ-ray spectrum detected during the full experiment after recoil selection. The spectrum in the bottom panel is from events selected with an addtional tag on the characteristic alpha decay energy of ^{107}Te.

RDT is a powerful technique used for in-beam studies of excited states in heavy neutron-deficient nuclei and its power is illustrated by Fig. 4.2. It has been one of the principal experimental techniques for studying such nuclei at the limits of stability. Presently, in-beam spectroscopy can be achieved for nuclei with production cross-sections as low as 10 nb [38]. In the proton-rich region, many nuclei decay by emitting protons or α particles which are ideal and most common for applying RDT since these decays take place in the same DSSD position as the implanted recoil and deposit their energy entirely. In some cases, it is also possible to use β decays as a tag [39]. Another alternative to the typical RDT technique is recoil-isomer tagging [40], in which isomeric γ-transitions are detected in the Planar strip or the Clover germanium detectors at the focal plane after the recoil implantation in the DSSD. In this thesis work, recoil-isomer tagging was applied for the identification of the prompt γ-rays of ^{169}Os used in the lifetime analysis. The lifetime of the isomer has to be sufficiently long such that the recoil can pass through the separator ($\sim 0.5\ \mu s$) and on the other hand, it must not be too long in order to be cleanly associated with recoil implantation ($\leq$ ms). The search time window between the recoil and the tag is normally chosen to be around three half-lives of the decay state of interest.

4.4 Identification of New Alpha Decays

Conversely, RDT can contribute to identifying previously unknown decay modes as well. As in the case of ^{171}Os, by using the known prompt γ-rays of the $\nu i_{13/2}$ band, it can be determined that the band-head state also has an alpha decay branch. Due to the incomplete charge collection effect of the DSSD, weak α decays at lower energy can be concealed by the continuous background from higher-energy decays. With the coincidence between α and the delayed γ-rays, we can overcome this problem and resolve weak α decays to study the fine structure, as shown in Figure 4.3 related to the newly identified α decays of ^{172}Ir. In the present results, the delayed γ-rays were measured using the planar HPGe detector at the focal plane and the absolute efficiency used for the correction of the γ-ray intensity was determined using GEANT4 Monte Carlo simulations [41].

4.5 Mass-to-Charge Ratios

In addition to the measurements of energies and half-lives for alpha or proton decays (which contribute to identifying new isotopes), additional information on the mass of the recoil of interest can provide further aid for the identification. The ion separator MARA has the ability to separate the fusion products according to their mass to electric charge state ratio m/q at the focal plane. The determination of the m/q value for each recoil is based on its x coordinate recorded by the MWPC. The electric and magnetic fields of MARA are optimized for the transmission of a reference ion with kinetic energy E_k, mass m_{ref} and charge state q_{ref} to the central position of the x plane of the MWPC. As used in the experiment resulting in the

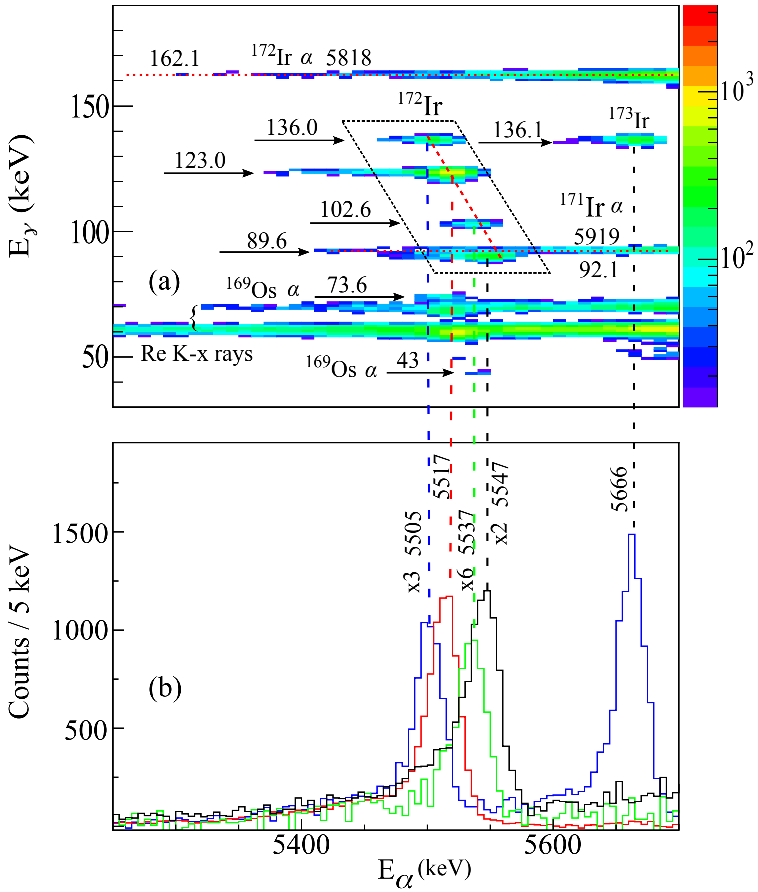

Figure 4.3: (a) $E_\alpha - E_\gamma$ coincidence spectrum with the time interval of $0 < \triangle t$ (γ - α) < 300 ns, where the delayed γ rays were detected by the planar detector at the focal plane and the α decays were measured with the DSSD. Each group is indicated with the corresponding energies, including the groups at the γ energies of 92.1 keV and 162.1 keV associated with the respective ^{171,172}Ir isotopes, and the group at α(5666 keV)-γ(136.1 keV) related to ^{173}Ir, as well as the groups at the γ energies of 43 keV and 73.6 keV correlated with the α decays of ^{169}Os. The parallelogram region indicates the newly identified α decays from the low-spin isomeric state of ^{172}Ir. (b) Projections on the E_α axis of the events from the ^{172}Ir region of (a) by gating on the respective delayed γ-ray. Relevant peaks are labeled with their corresponding E_α values. The intensity scale for the three weaker spectra is scaled up for better visibility.

identification of the new isotope ^{116}La, MARA was operated with the reference values $m_{ref} = 117$, $q_{ref} = 30.5^+$, and $E_k = 142$ MeV. Then the m/q value can be derived from the corresponding coordinate x, using the relation

$$\begin{aligned} \frac{m}{q} &= \frac{m_{ref}}{q_{ref}}(1 + \delta_{mpq}) \\ \delta_{mpq} &= \frac{\delta x_m}{D \times 100} \end{aligned} \tag{4.1}$$

where the parameter D is the dispersion at the focal plane of MARA and $D =$ 8 mm/(% change in m/q value) which means a 1% change in m/q value will introduce an 8 mm deviation from the position of the reference ion, and the δx_m is the relative difference in the experimentally measured x-coordinate and the δ_{mpq} is the corresponding relative difference in m/q for the ion of interest compared to the reference recoil. The centroid of the mass distribution for each charge state can then be obtained.

The recoils of interest cannot be resolved from the isobars solely based on the mass information. In some cases, mass distributions overlap with each other due to m/q ambiguities. However, this problem can usually be addressed effectively by combining the mass information with the multiplicity of evaporated charged particles detected by the JYTube detector at the target position.

4.6 Half-Life Measurements

The absolute time stamp information for each detector recorded by the TDR system can be used to measure the half-lives of nuclear states which decay by charged particle emission or by isomeric γ-rays. By applying an energy gate on the decay of interest and searching back to correlate with the time at which the recoil was implanted, the time difference spectrum can be extracted. One method to extract the half-life is by fitting a superposition of exponential functions due to the feature of the Poisson distribution [42], as follows

$$N = A \exp^{(-\lambda t)} + B \exp^{(-rt)} . \tag{4.2}$$

Here, N is the number of counts for each channel in the time distribution histograms. The parameter λ is the decay constant and the r is related to the random background events. Both parameters can be obtained from the fitting, and in the charged-particle decay, the background rate can be roughly estimated from the recoil rate per pixel in the DSSD. Then, the half-life can be obtained by

$$t_{1/2} = \frac{\ln 2}{\lambda}. \tag{4.3}$$

An example is shown in Figure 4.4 related to the determination of the half-life for the 227 keV isomeric-γ transition of ^{116}I.

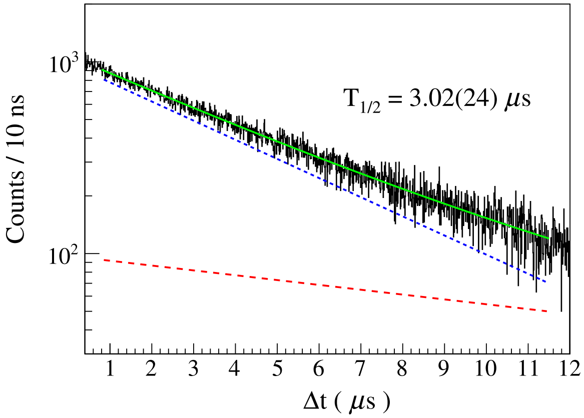

Figure 4.4: Time difference spectrum between the ^{116}I recoil implantation and detection of its 227 keV isomeric-γ transition as well as a least-squares fit applied (solid green line) comprised of an exponential fit for the component of interest (blue dashed line) and an exponential fit for the background component (red dashed line).

Another method specific for low statistics analysis is the Maximum Likelihood method [43]. If n decays happen at respective times $t_1, t_2, ..., t_n \leq$ the search time T, the probability of observing one decay during the time initerval t to $t + dt$ is given as

$$P(\lambda, t)dt = \lambda e^{-\lambda t} dt (1 - e^{-\lambda T})^{-1}. \tag{4.4}$$

Then, the probability to observe all the n decays is

$$P(\lambda, t_1, ..., t_n) = \prod_{i=1}^{n} P(\lambda, t_i). \tag{4.5}$$

By requiring it to have a maximum probability, namely

$$\frac{\partial \log P(\lambda, t_1, ..., t_n)}{\partial \lambda} = 0. \tag{4.6}$$

Then we can obtain the decay constant expression,

$$\frac{1}{\lambda} = \frac{1}{n} \sum_{i=1}^{n} (t_i) + \frac{T}{e^{\lambda T} - 1}. \tag{4.7}$$

If the search time T is long enough, this formula can be simplified to

$$\tau = \frac{1}{\lambda} = \frac{1}{n} \sum_{i=1}^{n} (t_i). \tag{4.8}$$

If the mean lifetime τ is not very short compared to the search time T, a correction has to be taken into account, which is obtained by iterating eq. 4.7 until it converges. The uncertainties of the half-lives determined with the Maximum Likelihood method are given by [44]

$$\tau_u \approx \frac{\tau}{1-\frac{1}{\sqrt{n}}}, \quad \tau_l \approx \frac{\tau}{1+\frac{1}{\sqrt{n}}} \tag{4.9}$$

in which τ_u and τ_l stand for the upper and lower uncertainty limits of the life time, respectively. In the case of an extensive time span, treating the time distribution with sufficient statistics in a linear time scale is challenging. Instead, an alternative method is to transform the linear time spectrum to a logarithmic time scale [44,45]. This method can sometimes more clearly divide the time distribution spectrum into two components and the random background can be isolated from the main intensity, as shown in Fig. 4.5 related to the lifetime fitting of the 5306 keV α decay of ^{171}Os. The two-component logarithmic function is given by

$$|\frac{dn}{d\theta}| = (n_1\lambda_1 e^{-\lambda_1 e^{\theta}} + n_2\lambda_2 e^{-\lambda_2 e^{\theta}})e^{\theta}. \tag{4.10}$$

where $\theta = ln(\triangle \mathrm{t})$ and $\triangle$t is the correlation time between decay and recoil and in the unit of ms, n_i and λ_i are the number of counts and decay constants corresponding to the true and random-correlated distributions as shown in Fig. 4.5. The lifetime τ determines the position of the primary peak and ln(τ) corresponds to the most likely temporal location in the distribution. The half-lives measured in this thesis have mainly relied on the Maximum Likelihood method in the logarithmic time scale.

4.7 Lifetime Measurements of Excited States

The lifetime measurements of nuclear excited levels have long provided fundamental information for our understanding of nuclear properties, such as shapes and collective degrees of freedom. The resulting reduced transition probability directly reflects the overlap between the wave functions of the initial and final quantum states in a nucleus and gives insight into the structural properties. There are many experimental techniques available to measure lifetimes of excited states. Two methods based on the Doppler effect are widely employed to measure very short lifetimes (10^{-9} to 10^{-14} s) [46], i.e., the Doppler-shift attenuation method (DSAM) ($\sim$ 0.01 to 1 ps) and the Recoil Distance Doppler Shift (RDDS) method ($\sim$ 1 ps to 1 ns) [47]. In this work, the RDDS method was used and its analysis is presented in the following subsections.

4.7.1 RDDS Method

The idea of the RDDS method is to relate the lifetime τ of an excited state of interest to the flight time t of the recoiling nucleus at the time of the emission of

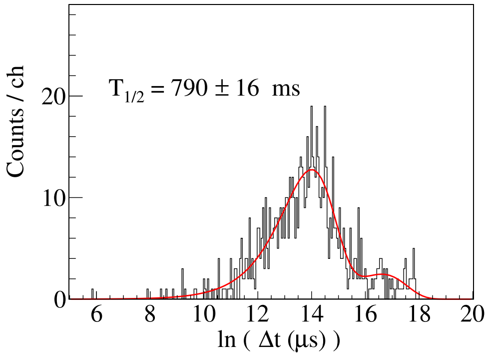

Figure 4.5: Logarithmic time spectrum of the 5306 keV alpha decay events in correlation with ^{171}Os recoils, fitted with a two-component function (red). The time window for the recoil-α correlation was set to 1 min. The smaller distributions at higher ln(△t) values are due to the random correlated background with its effective fitted half-life.

a γ ray. The excited states, can for example, be populated in heavy-ion induced fusion evaporation reactions using a thin target from which the excited nuclei recoil out. After traveling a certain distance d at a velocity v_1, the recoils are slowed down by a degrader foil to a smaller velocity v_2 before being transported into the separator RITU.

If the γ-ray is emitted while the nucleus is in flight, the Doppler effect will give rise to an energy shift of the observed γ-ray, which is expressed by:

$$E_\gamma = E_0 \frac{\sqrt{1-\beta^2}}{1-\beta cos\theta} \approx E_0(1+\beta\ cos\theta). \tag{4.11}$$

where θ is the angle in the laboratory system between the direction of the γ-emission and the flight direction of the recoiling nuclei with the velocity of v, E_0 is the γ-ray energy of the nucleus at rest, and $\beta = v/c$ where c is the velocity of light. This effect shifts the γ-ray energies from the states of interest emitted before and after the degrader by different amounts, resulting in one fully shifted component and one degraded component in the γ-ray spectrum. By measuring the change of the intensities of both components with the distance between the target and the degrader, the lifetime of the nuclear level can be deduced.

In the Recoil Distance Doppler-Shift technique [48], a plunger device is used to mount a degrader foil behind the target to slow down the recoiling nuclei. This is illustrated in Fig. 4.6.

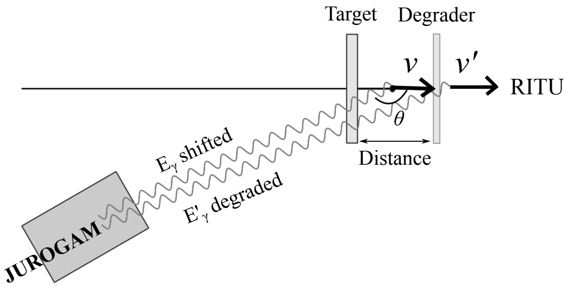

Figure 4.6: A schematic illustration of the principle of the RDDS method, adapted from the reference [48].

4.7.2 DDCM Method

In order to optimize the analysis of the RDDS data, the Differential Decay Curve Method (DDCM) was developed and tested by the University of Cologne group [49, 50]. The principle can be understood as follows. The excited level of interest, L_i, is depopulated via the transitions $L_i \rightarrow L_j$ in which j denotes a lower-lying state. On the other hand, the level L_i is populated via a number of transitions $L_h \rightarrow L_i$, where h denotes a higher-lying excited state. The relationship between the numbers of nuclei in the excited states L_i and L_h, i.e. $n_i(t)$ and $n_h(t)$, respectively, at the time t obey the following well-known differential equation:

$$\frac{dn_i(t)}{dt} = -\lambda_i n_i(t) + \sum_h b_{hi}\lambda_h n_h(t), \tag{4.12}$$

where λ_h and λ_i are the decay constants of the feeding and depopulating transitions, respectively, and b_{hi} represents the normalized branching ratio for the decay from the level L_h obtained by the measured relative γ-ray intensity. In practical situations, the intensity of a transition is always measured over a period of time. Integration of equation 4.12 over a period of time $t' > t$ gives:

$$\int_t^\infty \frac{dn_i(t')}{dt'}dt' = \lambda_i \int_t^\infty n_i(t')dt' + \sum_h b_{hi}\lambda_h \int_t^\infty n_h(t')dt' \tag{4.13}$$

and with

$$N_i(t) = -\lambda_i \int_t^\infty n_i(t')dt' \tag{4.14}$$

and

$$N_{hi}(t) = \lambda_h b_{hi} \int_t^\infty n_h(t')dt'. \tag{4.15}$$

Assuming finite lifetimes (i.e. $n(\infty) = 0$) one obtains :

$$-n_i(t) = -N_i(t) + \sum_h N_{hi}(t). \tag{4.16}$$

The quantities $N_{hi}(t)$ and $N_i(t)$ are proportional to the degraded components of the feeding and depopulating transitions, respectively, measured at the flight time t. By substituting the derivative of Eq. 4.14, Eq. 4.16 can be rewritten to

$$\tau_i = \frac{1}{\lambda_i} = \frac{-N_{ij}(t) + b_{ij}\sum_h N_{hi}(t)}{dN_{ij}(t)/dt} \tag{4.17}$$

with $N_{ij}(t) = b_{ij}N_i(t)$, which is regarded as the general form of the DDCM for the analysis in both singles plunger measurement and coincidence plunger measurement [48, 49]. Using the transformation of the flight times t to distances x, $t = x/v$, where v is the recoil velocity, the functions $N_{ij}(t)$ can be replaced by $N_{ij}(x)$. From the spectrum for each distance, one can directly measure the areas of the degraded components $I^d(x)$ and shifted components $I^s(x)$ in the peaks in the spectra corresponding to the transitions of interest. The relative quantity $Q_{ij}(x)$ is introduced by the relationship between the measurable quantities,

$$Q_{ij}(x) = \frac{N_{ij}(x)}{N_{ij}(0)} = \frac{I^d_{ij}(x)}{I^d_{ij}(x) + I^s_{ij}(x)}, \tag{4.18}$$

which is proportional to $N_{ij}(x)$. Then in the singles analysis of the RDDS data for a level of interest, i, the lifetime eq.4.17 can be written as:

$$\tau_i(x) = -\frac{Q_{ij}(x) - b_{ij}\sum_h (J_{hi}/J_{ij})Q_{hi}(x)}{\frac{d}{dx}Q_{ij}(x)}\frac{1}{v}, \tag{4.19}$$

where J_{hi}, J_{ij} are the relative intensities for the feeding $h \to i$ and depopulating $i \to j$ transitions, respectively.

In the singles RDDS data, measuring all possible feeding transitions is usually practically impossible since there can be weak feeding branches below the detection limit, e.g., from unobserved discrete levels. Therefore, the effect of unobserved feeding transitions to the level of interest has to be considered in the analysis. In certain cases where the observed feeding times are not particularly long compared with the depopulating transition and the intensity of the unobserved feeding is small, it is reasonable to assume that the unobserved feeding has a similar time behavior as the observed feeding [48, 49]. This hypothesis has been found to be realistic and validated using coincidence analysis in several measurements [51, 52]. Moreover, its validity can be checked directly by inspecting whether the general trend of lifetime values obtained at each distance deviates significantly from a horizontal line. In order to reduce systematic errors present in the analysis of singles plunger measurements, $\gamma-\gamma$ coincidence measurements can be introduced to avoid these problems [53]. The influence of the unobserved feeding on lifetime determination also can be effectively excluded. However, this type of measurements is always limited by statistics and a large enough reaction cross-section.

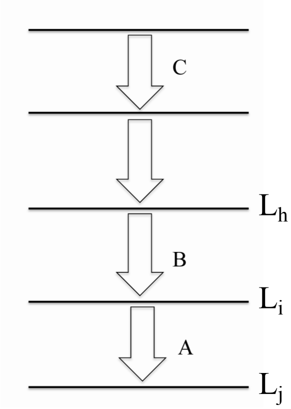

Figure 4.7: De-excitation scheme for coincidence DDCM.

Coincidence DDCM

In the case of coincidence data, the lifetime can be determined from gated spectra and two types of gating can be used, on a depopulating transition or on a feeding transition. Gating on a depopulating transition can help to reduce the background in the gated spectra whilst it does nothing to avoid potential problems with unobserved feeding. The method for the determination of the lifetime is the same one as used in the singles case. Gating on feeding transitions is a more powerful tool to avoid problems caused by indeterminate intensities or unobserved feedings. Using this approach, one can choose the decay path to avoid the problems aroused by unobserved feeding transitions or by the contamination of the doublet. As shown in Fig. 4.7, a cascade of γ-transitions is assumed to be observed almost simultaneously. The overall coincidence intensity between the transitions B and A can be regarded as the sum of partial coincidences:

$$(B_0^\infty, A_0^\infty) = (B_0^t, A_0^t) + (B_0^t, A_t^\infty) + (B_t^\infty, A_0^t) + (B_t^\infty, A_t^\infty). \tag{4.20}$$

For instance, the term (B_0^t, A_0^t) refers to the coincidence between the fully shifted components of the feeding transition B and the depopulating transition A and the term (B_t^∞, A_t^∞) represents the coincidence between the degraded components of the B and A transitions. The term $(B_t^\infty, A_0^t) = 0$ as a result of the time ordering i.e., that the detection of the degraded component of the populating transition cannot be associated with coincident detection of the fully shifted component of the depopulating transition.

Similarily as in eq. 4.17, the lifetime of level L_i can be determined using the following equation [48]:

$$\tau_i = \frac{-(B_0^\infty, A_t^\infty) + (B_t^\infty, A_0^\infty)}{\frac{d}{dt}(B_0^\infty, A_t^\infty)} \tag{4.21}$$

Since (B_0^∞, A_0^∞) is independent of time (i.e., the target-degrader distance), a general solution can be derived from the Eq. 4.21 with the transformation from the flight times to distances as

$$\tau_i(x) = \frac{(B_s, A_d)(x)}{\frac{d}{dx}(B_s, A_s)(x)} \frac{1}{v}. \tag{4.22}$$

where s and d stand for the fully shifted component and degraded component, respectively, and v is the mean velocity of the recoils before the degrader. In some situations, a gate on the fully shifted component of the direct feeding transition is not possible either because the low transition energy prevents one from unambiguously separating it from the degraded component, or due to the contamination from the energy similarity of other transitions. Alternatively, other feasible approaches can then be employed by gating on the shifted component of a higher-lying transition C (if clearly separated) as shown in Fig. 4.7 or by gating on both components of the transition C. For the latter case, the lifetime of the state of interest L_i can be obtained using the expression:

$$\tau_i(x) = \frac{-(C, A_u)(x) + (C, B_u)(x)\frac{(C,A)}{C,B}}{\frac{d}{dx}(C, A_u)(x)} \frac{1}{v}. \tag{4.23}$$

In addition, this expression also works for summing gates on several higher transitions together in order to obtain higher statistics. For the determination of the denominator part, i.e., the derivative $\frac{d}{dx}(B_s, A_s)$ as a function of the distance, the APATHIE software [54] was used in this thesis, which is based on the fitting of multiple consecutive derivable second-order polynomials.

Chapter 5

Summary

This chapter briefly summarizes the experimental results and the author's contributions to **papers I** to **IV**.

5.1 Paper I

Lifetime measurements for the excited states in the $\nu i_{13/2}$ yrast bands of the neutron-deficient osmium isotopes ^{169,171,173}Os have been measured for the first time using the DPUNS device combined with the Jurogam II array and employing the recoil-distance Doppler shift technique. The population of excited states in these nuclei was achieved via the ^{92}Mo(^{83}Kr, $2p4n$)^{169}Os, ^{92}Mo(^{83}Kr, $2p2n$)^{171}Os and ^{92}Mo(^{83}Kr, $2p$)^{173}Os fusion-evaporation reactions. The lifetimes of the first excited $17/2^+$ and $21/2^+$ states in ^{169,173}Os and the $29/2^+$ excited state in ^{171}Os were extracted based on the singles DDCM analysis method, and the lifetimes of the first excited $17/2^+$, $21/2^+$ and $25/2^+$ states in ^{171}Os were extracted based on the coincidence DDCM analysis method. The corresponding B(E2) values for the $21/2^+ \rightarrow 17/2^+$ and $17/2^+ \rightarrow 13/2^+$ electromagnetic transitions follow similar trends as observed in the neighboring even-N osmium isotopes, indicating that the $\mathrm{i}_{13/2^+}$ valence nucleon acts as a "spectator" with no or little influence on the nuclear shape or dynamics. An unusually low value is observed for the ratio $B(E2; 21/2^+ \rightarrow 17/2^+)/B(E2; 17/2^+ \rightarrow 13/2^+)$ in ^{169}Os, similarly to the "anomalously" low values of the ratio $B(E2; 4_1^+ \rightarrow 2_1^+)/B(E2; 2_1^+ \rightarrow 0_{\mathrm{gs}}^+)$ found for several neighbouring even-even transitional rare-earth nuclides. Such low ratios of electromagnetic quadrupole strength are highly unexpected in the nuclei far from closed shells and can not be accounted for by state-of-the-art theoretical models.

5.2 Paper II

Excited states in the extremely neutron-deficient nucleus ^{107}Te have been identified from two separate experiments, one using the reaction ^{54}Fe(^{58}Ni, $2p3n$)^{107}Te at the beam energy of 215 MeV based on the vacuum-mode separator MARA and the other one using the reaction ^{58}Ni(^{54}Fe, $2p3n$)^{107}Te at the beam energy of 195 MeV based on the gas-filled separator RITU. Prompt γ-rays associated with ^{107}Te were identified with the recoil-decay tagging technique and two distinct structures were tentatively assigned to be built on the $\nu h_{11/2}$ and $\nu g_{7/2}$ quasiparticle states. The structures have been compared with large-scale shell model calculations and the corresponding deformations for the positive and negative parity have been calculated using the total Routhian surface method. It is suggested that a neutron occupying the $h_{11/2}$ intruder orbit has a shape-polarizing effect towards larger quadrupole deformation (β_2) as the $N = 50$ shell closure is approached, leading to a stronger collectivity than for the positive-parity $d_{5/2}$ and $g_{7/2}$ configurations.

5.3 Paper III

The most neutron deficient lanthanum isotope known to date, ^{116}La, has been discovered via its ground-state proton emission ($E_p = 718(9)$ keV, $T_{1/2} = 50(22)$ ms). The ^{116}La nuclei were produced in the fusion-evaporation reaction ^{58}Ni(^{64}Zn, p5n)^{116}La and identified via their proton radioactivity using the MARA mass spectrometer and the silicon detector placed at its focal plane, in conjunction with the JYTUbe detector at the target position. The proton decay of ^{117}La has been remeasured ($E_p = 808(3)$ keV, $T_{1/2} = 21.6(31)$ ms) and the observations of γ decays from isomeric states in ^{116}La and ^{117}La are also reported. The proton emission probabilities have been calculated using the Universal Decay Law approach and it is found that the emission probability in ^{116}La is enhanced compared to the less exotic nearest neighbouring isotope (^{117}La) while the proton-emission Q-value is lower. These unexpected findings are proposed as a possible manifestation of strong neutron-proton pairing of the isovector type which might facilitate the emission of the proton since such correlations are predicted to peak at the nuclear surface.

5.4 Paper IV

In the same experimental data as used in **Paper I**, new α-decay fine structures have been identified for ^{171,172}Os and ^{171,172,174}Ir, respectively. In total, 13 new α lines have been resolved and two new γ-ray transitions have been observed by means of $E_\alpha - E_\gamma$ correlations. The formation amplitudes for the new α decays obtained in this work were calculated using the Universal Decay Law formula. The reduced widths for these decays were calculated using the traditional Rasmussen approach. Hindrance factors have been evaluated by taking the ground state α decay of ^{170}Os as the reference. A somewhat enhanced hindrance factor is observed for the newly measured α-decay branch of ^{172}Os to the first excited 2^+ state in ^{168}W. This is suggested to be a result of coexistence between configurations with different shapes in the daughter nucleus. Mean field total Routhian surface calculations support this picture and indicate that the observed α-decay fine structure is sensitive to rather subtle differences in the shape parameters of the final states. Shape coexistence may also be a factor behind the increased hindrance factors observed for some of the new α-decay branches in the odd-Z or odd-A nuclides, but in these cases, the theoretical interpretation requires further studies.

5.5 Author's Contributions

A brief summary of the author's contributions to the four papers is presented below.

Paper I: The author of this thesis performed the offline data analysis and was the principal author of the paper.

Paper II: This study contains two experimental data sets; the first one based on RITU was performed in the year 2006 and the second one based on MARA was performed in 2019. The author of this thesis participated in the second experiment, performed the offline data analysis using the two data sets, and was the principal author of the paper.

Paper III: The author of this thesis participated in the experiment, performed the offline data analysis, and was the principal author of the paper.

Paper IV: The author of this thesis performed the offline data analysis and was the principal author of the paper.

Bibliography

[1] T. Bäck, "Spectroscopy of neutron deficient nuclei in the A = 90 and A = 170 mass regions," Ph.D. dissertation, KTH, 2002.

[2] D. L. Hill and J. A. Wheeler, "Nuclear Constitution and the Interpretation of Fission Phenomena," *Phys. Rev.*, vol. 89, pp. 1102–1145, 1953.

[3] G. Audi, O. Bersillon, J. Blachot, and A. H. Wapstra, "The NUBASE evaluation of nuclear and decay properties," *Nuclear physics A*, vol. 729, pp. 3–128, 2003.

[4] K. S. Krane, *Introductory nuclear physics.* John Wiley & Sons, 1991.

[5] G. Gamow, "Zur quantentheorie des atomkernes," *Zeitschrift für Physik*, vol. 51, pp. 204–212, 1928.

[6] J. O. Rasmussen, "Alpha-decay barrier penetrabilities with an exponential nuclear potential: even-even nuclei," *Physical Review*, vol. 113, p. 1593, 1959.

[7] G. Igo, "Optical model potential at the nuclear surface for the elastic scattering of alpha particles," *Physical Review Letters*, vol. 1, p. 72, 1958.

[8] R. Thomas, "A formulation of the theory of alpha-particle decay from time-independent equations," *Progress of Theoretical Physics*, vol. 12, pp. 253–264, 1954.

[9] R. G. Lovas, R. Liotta, A. Insolia, K. Varga, and D. Delion, "Microscopic theory of cluster radioactivity," *Physics reports*, vol. 294, pp. 265–362, 1998.

[10] D. S. Delion, *Theory of particle and cluster emission.* Springer, 2010, vol. 819.

[11] C. Qi, R. Liotta, and R. Wyss, "Recent developments in radioactive charged-particle emissions and related phenomena," *Progress in Particle and Nuclear Physics*, vol. 105, pp. 214–251, 2019.

[12] C. Qi, F. R. Xu, R. J. Liotta, and R. Wyss, "Universal decay law in charged-particle emission and exotic cluster radioactivity," *Phys. Rev. Lett.*, vol. 103, p. 072501, 2009.

[13] B. Blank and M. Borge, "Nuclear structure at the proton drip line: Advances with nuclear decay studies," *Progress in Particle and Nuclear Physics*, vol. 60, pp. 403–483, 2008.

[14] A. N. Bohr and B. R. Mottelson, *Nuclear Structure (In 2 Volumes).* World Scientific Publishing Company, 1998.

[15] T. Kibedi, T. Burrows, M. B. Trzhaskovskaya, P. M. Davidson, and C. W. Nestor Jr, "Evaluation of theoretical conversion coefficients using BrIcc," *Nuclear Instruments and Methods in Physics Research Section A*, vol. 589, pp. 202–229, 2008.

[16] R. Casten and R. F. Casten, *Nuclear structure from a simple perspective.* Oxford University Press, 2000, vol. 23.

[17] "http://nucalf.physics.fsu.edu/∼riley/gamma/gamma2-5.html," Gammasphere online booklet.

[18] C. R. Alvarez, "The GASP array," *Nuclear Physics News*, vol. 3, pp. 10–13, 1993.

[19] C. Beausang, S. Forbes, P. Fallon, P. Nolan, P. Twin, J. Mo, J. Lisle, M. Bentley, J. Simpson, F. Beck *et al.*, "Measurements on prototype Ge and BGO detectors for the eurogam array," *Nuclear Instruments and Methods in Physics Research Section A*, vol. 313, pp. 37–49, 1992.

[20] G. Duchêne, F. Beck, P. Twin, G. De France, D. Curien, L. Han, C. Beausang, M. Bentley, P. Nolan, and J. Simpson, "The clover: a new generation of composite ge detectors," *Nuclear Instruments and Methods in Physics Research Section A*, vol. 432, pp. 90–110, 1999.

[21] J. Pakarinen, J. Ojala, P. Ruotsalainen, H. Tann, H. Badran, T. Calverley, J. Hilton, T. Grahn, P. Greenlees, M. Hytönen *et al.*, "The JUROGAM 3 spectrometer," *The European Physical Journal A*, vol. 56, pp. 1–8, 2020.

[22] J. Henderson, P. Ruotsalainen, D. Jenkins, C. Scholey, K. Auranen, P. Davies, T. Grahn, P. Greenlees, T. Henry, A. Herzáň *et al.*, "Enhancing the sensitivity of recoil-beta tagging," *Journal of Instrumentation*, vol. 8, p. P04025, 2013.

[23] D. Jenkins, *Radiation Detection for Nuclear Physics.* IOP Publishing, 2020.

[24] J. Uusitalo, J. Sarén, J. Partanen, and J. Hilton, "Mass analyzing recoil apparatus, MARA," *Acta Physica Polonica B*, vol. 50, 2019.

[25] L. Sottili, "Test of jyutube as a veto detector at MARA for background suppression in nuclear spectroscopy beyond the proton drip line," 2018.

[26] M. Leino, J. Äystö, T. Enqvist, P. Heikkinen, A. Jokinen, M. Nurmia, A. Ostrowski, W. Trzaska, J. Uusitalo, K. Eskola *et al.*, "Gas-filled recoil separator for studies of heavy elements," *Nuclear Instruments and Methods in Physics Research Section B*, vol. 99, pp. 653–656, 1995.

[27] M. Leino, "In-flight separation with gas-filled systems," *Nuclear Instruments and Methods in Physics Research Section B*, vol. 126, pp. 320–328, 1997.

[28] "https://www.jyu.fi/science/en/physics/research/infrastructures/accelerator-laboratory/nuclear-physics-facilities/recoil-separators."

[29] A. Ghiorso, S. Yashita, M. Leino, L. Frank, J. Kalnins, P. Armbruster, J.-P. Dufour, and P. Lemmertz, "Sassy, a gas-filled magnetic separator for the study of fusion reaction products," *Nuclear Instruments and Methods in Physics Research Section A*, vol. 269, pp. 192–201, 1988.

[30] J. Sarén, "The ion-optical design of the mara recoil separator and absolute transmission measurements of the ritu gas-filled recoil separator," 2011.

[31] J. Saren, J. Uusitalo, M. Leino, P. Greenlees, U. Jakobsson, P. Jones, R. Julin, S. Juutinen, S. Ketelhut, M. Nyman *et al.*, "The new vacuum-mode recoil separator MARA at JYFL," *Nuclear Instruments and Methods in Physics Research Section B*, vol. 266, no. 19-20, pp. 4196–4200, 2008.

[32] R. Page, A. Andreyev, D. Appelbe, P. Butler, S. Freeman, P. Greenlees, R.-D. Herzberg, D. Jenkins, G. Jones, P. Jones *et al.*, "The GREAT spectrometer," *Nuclear Instruments and Methods in Physics Research Section B*, vol. 204, pp. 634–637, 2003.

[33] M. Taylor, D. Cullen, A. Smith, A. McFarlane, V. Twist, G. Alharshan, M. Procter, T. Braunroth, A. Dewald, E. Ellinger *et al.*, "A new differentially pumped plunger device to measure excited-state lifetimes in proton emitting nuclei," *Nuclear Instruments and Methods in Physics Research Section A*, vol. 707, pp. 143–148, 2013.

[34] L. Cleemann, J. Eberth, W. Neumann, N. Wiehl, and V. Zobel, "A plunger device with a piezoelectric fine adjustment and a pll distance regulation," *Nuclear Instruments and Methods*, vol. 156, pp. 477–482, 1978.

[35] P. Rahkila, "Grain—a java data analysis system for total data readout," *Nuclear Instruments and Methods in Physics Research Section A*, vol. 595, pp. 637–642, 2008.

[36] A. Krulisch and R. Axtmann, "Energy dependence of the pulse height defect in silicon particle detectors," *Nuclear Instruments and Methods*, vol. 55, pp. 238–248, 1967.

[37] E. Paul, P. Woods, T. Davinson, R. Page, P. Sellin, C. Beausang, R. Clark, R. Cunningham, S. Forbes, D. Fossan *et al.*, "In-beam γ-ray spectroscopy above Sn 100 using the new technique of recoil decay tagging," *Physical Review C*, vol. 51, p. 78, 1995.

[38] P. Rahkila, D. Jenkins, J. Pakarinen, C. Gray-Jones, P. Greenlees, U. Jakobsson, P. Jones, R. Julin, S. Juutinen, S. Ketelhut *et al.*, "Shape coexistence at the proton drip-line: First identification of excited states in ^{180}Pb," *Physical Review C*, vol. 82, p. 011303, 2010.

[39] A. Steer, D. Jenkins, R. Glover, B. N. Singh, N. Pattabiraman, R. Wadsworth, S. Eeckhaudt, T. Grahn, P. Greenlees, P. Jones *et al.*, "Recoil-beta tagging: A novel technique for studying proton-drip-line nuclei," *Nuclear Instruments and Methods in Physics Research Section A: Accelerators, Spectrometers, Detectors and Associated Equipment*, vol. 565, pp. 630–636, 2006.

[40] C. Scholey, D. Cullen, E. Paul, A. Boston, P. Butler, T. Enqvist, C. Fox, H. Scraggs, S. Shepherd, O. Stezowski *et al.*, "Recoil isomer tagging in the proton-rich odd-odd n= 77 isotones, ^{142}Tb and ^{144}Ho," *Physical Review C*, vol. 63, p. 034321, 2001.

[41] A. Andreyev, P. Butler, R. Page, D. Appelbe, G. Jones, D. Joss, R.-D. Herzberg, P. Regan, J. Simpson, and R. Wadsworth, "Geant monte carlo simulations for the GREAT spectrometer," *Nuclear Instruments and Methods in Physics Research Section A*, vol. 533, pp. 422–434, 2004.

[42] B. Hadinia, "In-beam study of extremely neutron deficient nuclei using the recoil-decay tagging technique," Ph.D. dissertation, KTH, 2008.

[43] E. Segre, *Nuclei and particles: an introduction to nuclear and subnuclear physics.* WA Benjamin, 1974.

[44] K.-H. Schmidt, C.-C. Sahm, K. Pielenz, and H.-G. Clerc, "Some remarks on the error analysis in the case of poor statistics," *Zeitschrift für Physik A Atoms and Nuclei*, vol. 316, pp. 19–26, 1984.

[45] K.-H. Schmidt, "A new test for random events of an exponential distribution," *The European Physical Journal A*, vol. 8, pp. 141–145, 2000.

[46] P. Nolan and J. Sharpey-Schafer, "The measurement of the lifetimes of excited nuclear states," *Reports on Progress in Physics*, vol. 42, p. 1, 1979.

[47] A. Schwarzschild and E. Warburton, "The measurement of short nuclear lifetimes," *Ann. Rev. Nucl. Sci.*, vol. 18, pp. 265–287, 1968.

[48] A. Dewald, O. Möller, and P. Petkov, "Developing the recoil distance doppler-shift technique towards a versatile tool for lifetime measurements of excited nuclear states," *Progress in Particle and Nuclear Physics*, vol. 67, pp. 786–839, 2012.

[49] A. Dewald, S. Harissopulos, and P. Von Brentano, “The differential plunger and the differential decay curve method for the analysis of recoil distance doppler-shift data,” *Zeitschrift für Physik A Atomic Nuclei*, vol. 334, pp. 163–175, 1989.

[50] G. Böhm, A. Dewald, P. Petkov, and P. Von Brentano, “The differential decay curve method for the analysis of doppler shift timing experiments,” *Nuclear Instruments and Methods in Physics Research Section A*, vol. 329, pp. 248–261, 1993.

[51] P. Petkov, S. Harissopulos, A. Dewald, M. Stolzenwald, G. Böhm, P. Sala, K. Schiffer, A. Gelberg, K. Zell, P. Von Brentano *et al.*, “Picosecond lifetime measurements and collective transition strengths in ^{128}Ba,” *Nuclear Physics A*, vol. 543, pp. 589–612, 1992.

[52] P. Petkov, A. Dewald, R. Kühn, R. Peusquens, D. Tonev, S. Kasemann, K. Zell, P. von Brentano, D. Bazzacco, C. Rossi-Alvarez *et al.*, “Coincidence recoil-distance doppler-shift lifetime measurements in ^{128}Ba,” *Physical Review C*, vol. 62, p. 014314, 2000.

[53] S. Harissopulos, A. Dewald, A. Gelberg, P. Von Brentano, K. Loewenich, K. Schiffer, and K. Zell, “Lifetime measurements in ^{120}Xe, using a coincidence plunger technique,” *Nuclear Physics A*, vol. 467, pp. 528–538, 1987.

[54] F. Seiffert, “Program apathie,” *Institut für Kernphysik, Universitat zu Köln*, 1989 (unpublished).